Structural and diagenetic controls on flow pathways in fractured Triassic Muschelkalk and Keuper limestones, southern Germany – Implications for geoenergy exploration

Jasemin Ayse Ölmez *, Benjamin Busch, Christoph Hilgers

Institute of Applied Geosciences, Structural Geology & Tectonics, Karlsruhe Institute of Technology, Adenauerring 20a, 76131, Karlsruhe, Germany

ABSTRACT

Understanding structural and diagenetic interactions is key in analyzing flow pathways in tight lithologies in the focus of geo-energy production as e.g., geothermal energy. Fracture spacing and clustering is crucial for reservoir production success and reduces uncertainty in reservoir exploration and utilization. This outcrop analog study evaluates diagenesis, fractures, vein cement generations, kink bands, and faults in tight fractured limestones of the Upper Muschelkalk-Lower Keuper transition on the eastern Upper Rhine Graben shoulder in SW Germany. Early and burial diagenesis led to cementation of former pore spaces and therefore drastically reduced the matrix porosity and permeability (porosity: 0.13–10.87 %, permeability: <0.0001 mD to 9.7 mD). Highest permeabilities are recorded in samples containing partially sealed veins and stylolites (up to 9.7 mD) at 1.2 MPa confining stress. The impact of increasing confining stress on the permeability of undisturbed limestones, as well as limestones containing stylolites and partially sealed veins, indicate that besides an undisturbed host rock sample and a sample containing stylolites, partially sealed veins preserve higher permeability at 30 MPa confining stress (41 % of initial value, compared to 16 and 11 % of the initial value).

Fracture cluster analyses using the normalized correlation count method indicates that clustering around a breached kink band and associated fault is not symmetrically arranged and contains fracture sets of different strike. Fracture clusters also exist away from the fault at the breached kink band. Slip and dilation tendencies indicate that clustered fracture sets striking NNE-SSW parallel to the Rhine graben rift, WNW-ESE, and NW-SE parallel to the in-situ maximum principal horizontal stress are more likely to contribute to fluid flow as they are suitably oriented in the present-day stress field. Breached, decameter-scale reverse kink bands are the first reported in the region, c. 180–200 km N-NNE of the Alpine deformation front. Kink bands are most likely related to compression by far field stresses induced by the Alpine orogeny during the Eocene, and show partially cemented fault planes indicating locally persevered pore space.

The applied methods of structural and diagenetic reservoir quality assessment and obtained outcomes aid in the understanding of fluid migration pathways for geoenergy applications in the Upper Rhine Graben area. Further, the results are also transferrable to other fractured tight reservoirs worldwide, which can help to solve problems for energy or heat supply that are of societal importance.

1. Introduction

Porosity and permeability of carbonate reservoirs worldwide is affected by the depositional environment, diagenetic overprint resulting in a deterioration or enhancement by cementation, dissolution, and dolomitization, and fractures (e.g., Roehl and Choquette, 2012, their tables 1.1 and 1.2). Excellent matrix porosity and permeability can be retained in carbonates (e.g., Ehrenberg et al., 2006; Melzer and Budd, 2008), but where cementation reduced the fluid flow potential of a formation, fractures can be the dominant porosity type (Garland et al., 2012; Lamarche et al., 2012). Therefore, assessing the depositional environment, diagenetic alteration, and structural inventory is essential to understand porosity and permeability in carbonates. Fractures in reservoirs can enhance the local permeability and thus positively

influence production if not sealed. Fracture mineralization can result in increased uncertainty during reservoir development (e.g., Almansour et al., 2020), because sealed fractures can result in reservoir compartmentalization (Moore and Wade, 2013). However, fractured carbonates host a large amount of conventional reserves globally (Burchette and Britton, 1985; Burchette, 2012; Harbaugh, 1967), such as giant fields producing hydrocarbons as the Ghawar oil field in Saudi Arabia (Kosari et al., 2017), the Gachsaran oil field in Iran, Kirkuk in Iraq (Tavakoli, 2020) or pre-salt carbonate reservoirs of the Santos Basin at the Brazilian Atlantic margin (e.g., Wagner Moreira et al., 2023). Fractured carbonates are also relevant as energy storage sites such as Europe's largest gas storage site Rehden, Germany, with 3.95 bcm working gas at 1.9–2.3 km depth (LBEG, 2023), and supply drinking water for approximately 25 % of the world population worldwide, where the reservoir is found at 10s of meters depth (Medici et al., 2021; Suski et al., 2008). Furthermore, carbonate reservoirs are of recent interest for geothermal energy production. For example, deep geothermal exploration in the NW European Carboniferous Basin in the Netherlands and the Molasse Basin in Germany target fractures, faults and karstification (Gutteridge et al., 2025; Kaminskaite-Baranauskiene et al., 2023).

Fluid flow and surface area for heat exchange depend on permeable host rock porosity and the size and abundance of naturally occurring or engineered fractures. Additionally, fluid pathways depend on several factors such as the depositional environment and facies, rock-fabric, and the diagenetic overprint (Ahr, 2008; Burchette and Britton, 1985; Burchette, 2012; Worden et al., 2018). Diagenetic processes can cause cementation, calcification/dolomitization, but also dissolution of minerals, and/or compaction and formation of stylolites (Gomez-Rivas et al., 2022; Humphrey et al., 2019; Ölmez et al., 2024; Schoenherr et al., 2018), which increases the complexity in predicting petrophysical properties. Therefore, when assessing carbonate reservoirs, a combination of rock classification, diagenetic analysis, petrophysical analysis (e. g., Machel, 2005) and the assessment of the structural inventory provide constraints on reservoir properties and thus limit exploration risks (e.g., Becker et al., 2019b).

Open fractures (joints) in tight rocks may be preferred fluid pathways in the subsurface, and are therefore of increasing interest in research related to geothermal energy production, hydrocarbon recovery, gas storage, and groundwater reservoir assessment (Bahrami et al., 2012; Carlos de Dios et al., 2017; Elliott et al., 2025; Khelifa et al., 2014; Laubach et al., 2004). Although the ability of fractures to transmit fluids is widely considered to be principally governed by the current stress field (e.g., Barton et al., 1995; Finkbeiner et al., 1997; Mattila and Tammisto, 2012) in some cases the openness of fractures is relatively insensitive to small differences in confining pressures in the subsurface (Laubach et al., 2004) and mineral deposits in the fractures may be determinative of the capacity of fractures to support flow (e.g., Almansour et al., 2020; Olson et al., 2009).

Furthermore, the understanding of fracture spacing and clustering are important for the success or failure of production of reservoirs (Li et al., 2018; Marrett et al., 2018; Narr, 1996). Especially in tight formations (low matrix porosity and permeability), the reservoir is dominantly controlled by its fracture network (Agosta et al., 2010; Becker et al., 2018, 2019a; Elliott et al., 2025; Rashid et al., 2023). A combination of fracture data from outcrop studies and the subsurface help to understand fracture patterns and can be used for fractured reservoir modelling, and thus reduce uncertainties for geoenergy applications (Allgaier et al., 2023a; Becker et al., 2018).

Because data from the subsurface is scarce and mostly only allows the delineation of properties from a point source (i.e. individual plugs) or line-source (e.g., geophysical logs) in wells, outcrop analog studies can aid in understanding lateral variations (Becker et al., 2019a). Assuming that fractures formed as different generations over time with different strike orientations per generation, care has to be taken to only assess fractures with the same strike orientation (e.g., Li et al., 2018) when assessing fracture clustering and intensity. Tectonic processes

such as lateral compression, extension, fluid overpressure or uplift can cause fracturing and enhance flow properties (e.g., Moore and Wade, 2013) or affect pre-existing fractures by dilation or shearing in a present-day stress field (Ferrill et al., 2020; Morris et al., 1996), which can adjust fluid pathways in open and partially sealed veins. Especially partially sealed veins, occasionally preserving bridging textures, are interpreted to preserve permeability at depth (Gale et al., 2010; Lander and Laubach, 2015). However, the analysis especially of barren fractures in quarries does not necessarily reflect fracture intensities at depths (e. g., Becker et al., 2018; Li et al., 2018).

The Upper Rhine Graben hosts the largest geothermal anomaly in Germany (Clauser and Villinger, 1990; Pribnow and Schellschmidt, 2000) and is in the focus of geothermal exploration (Harlé et al., 2019; Heap et al., 2019; Kushnir et al., 2018). At the Soultz-sous-Forêts geothermal site in France, Lower and Middle Muschelkalk lithologies were studied with a focus on petrophysical, thermal, and geomechanical properties (Heap et al., 2019). So far, the Upper Muschelkalk lithologies were of interest in terms of facies and sequence stratigraphy (Aigner, 1985, 1986; Aigner and Bachmann, 1992; Brüderlin, 1970; Brunner and Simon, 1985; Geng, 1996; Geng and Zeeh, 1995; Hagdorn and Simon, 2021; Mehl, 1982; Seufert, 1984; Seufert and Schweizer, 1985; Vollrath, 1938; Zeeh and Geng, 2001). The Upper Muschelkalk carbonate platform in southern Germany has previously been used as an outcrop analog for carbonate reservoirs in the Middle East, e.g., Khuff, Hanifa, and Arab Formation due to conceptually comparable characteristics (Koehrer et al., 2012; Kostic and Aigner, 2004; Warnecke and Aigner, 2019). The petrophysical values can vary within microfacies types, therefore a grouping for petrophysical values with respect to facies types is not applicable in all regions (Kostic and Aigner, 2004). While the relation between microfacies types as a function of the depositional environment and petrophysical values has been shown, the relation of petrophysical values with diagenetic processes and the structural overprint is not established yet for the Southern Germanic Basin. Structural analysis of the Triassic Muschelkalk so far focused on fracture intensity related to the vicinity of normal, strike-slip, and reverse faults (Meier et al., 2015). However, successfully assessing the reservoir quality of limestones may be key in unlocking geothermal and hydrocarbon reservoir potential in the Upper Rhine Graben.

In this study, we first link lithological, petrographic, and petrophysical analyses to assess reservoir quality in limestones of the Upper Muschelkalk to Lower Keuper transition to fill the knowledge gap on primary porosity in relation to microfacies and diagenesis. We then assess the relation between petrophysical analyses with compressional and tensional deformation structures in form of (breached) conjugate reverse kink bands and different fracture and vein cement generations. We also determine the effect of increases in confining stress on the permeability of undisturbed limestones, and limestones containing stylolites, and partially sealed veins. As partially sealed veins contribute to the fluid flow network in fractured carbonate reservoirs and are discussed to preserve fluid pathways in unsuitable stress fields, the integration of structural diagenetic properties thus helps to understand the fluid flow system. In combination with structural and diagenetic assessments, fracture cluster analyses using the normalized correlation count (NCC) method, and slip tendency (T_s) and dilation tendency (T_d) evaluations, we evaluate the controlling factors on fluid pathways in carbonates. The studied quarry is located on the eastern Upper Rhine Graben shoulder in SW Germany and also contains breached, decameter-scale conjugate kink bands. Kink bands are tabular fold zones cutting foliation as e.g., bedding, where foliation is rotated as result from shear coupling and commonly occur as conjugate sets (box fold-like conjugate system) (Dewey, 1965) and are used as paleo-stress indicator in rocks (Srivastava et al., 1998). We assess the structural diagenetic properties of fractures, and their likely contribution to fluid flow, and evaluate their formation in reconstructed stress fields affecting the region.

The applied workflows and derived results contribute to the understanding of migration pathways of fluids for e.g., geothermal energy or

hydrocarbons in the Upper Rhine Graben and other fractured carbonates elsewhere.

2. Geological setting

The Muschelkalk was deposited in the southern Germanic Basin, following a northwards marine ingression into the basin (Fig. 1d), which was separated from the open-marine Tethys by the Vindelician/Bohemian Massif in the south (Aigner, 1985, 1986; Kostic and Aigner, 2004). Following the opening of the Burgundy gate, the East Carpathian gate and the Silesian-Moravian gate (Fig. 1d), the transgression during the Muschelkalk formed a gently inclined carbonate ramp comprising limestone, dolostone, claystone, and evaporite deposits (Kostic and Aigner, 2004). The transition to the Vindelician-Bohemian Massif during the Muschelkalk is characterized by coast-parallel deposition of terrestrial sediments (Aigner, 1985; Kostic and Aigner, 2004 and references

therein). The Muschelkalk limestones have been replaced by a dolomitic limestone facies towards the terrestrial sediments (Kostic and Aigner, 2004). The studied top part of the Upper Muschelkalk (Meißner Fm., LGRB, 2022) is characterized by an overall shallowing up sequence of a highstand systems tract at the end of the Muschelkalk and comprises an increasing amount of bioclastic, oolitic, and oncolitic beds and shows more intense dolomitization (Aigner and Bachmann, 1992). This regressive trend during the uppermost Muschelkalk continues into the Lower Keuper (Aigner and Bachmann, 1992). The overlying Keuper (Early Ladinian to Rhaetian) is characterized by transgressive and regressive deposits, which lead to the formation of clastic to transitional marine and evaporitic deposits (Ziegler, 1982). The lowermost Keuper (Erfurt Fm.) is present as claystone/dolomite intercalations, which may contain fine-to medium-grained sandstone beds. Furthermore, coaly layers and limey and phosphatic bonebeds can occur marking the lithostratigraphic boundary between the Muschelkalk and Keuper (Etzold
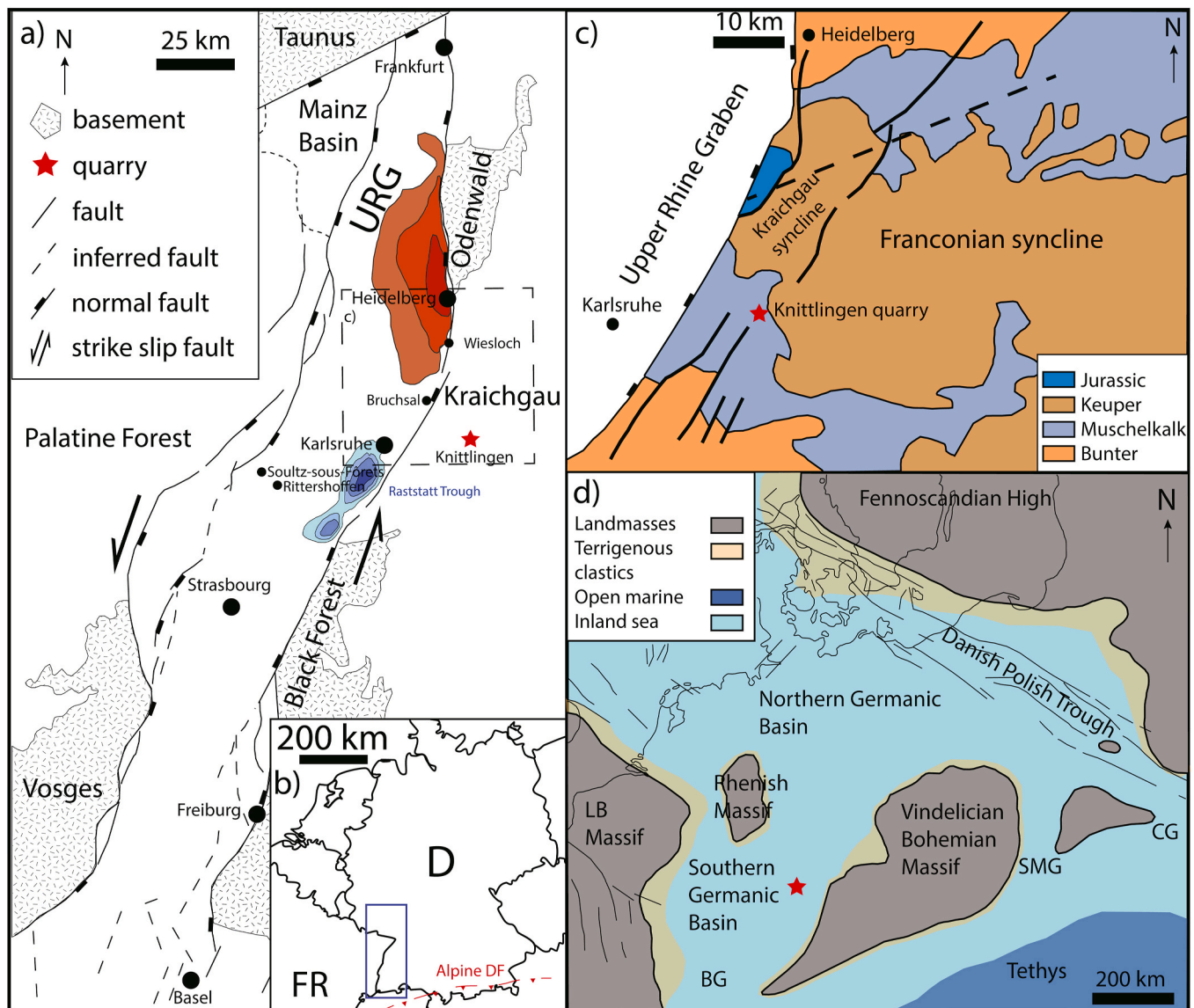

Fig. 1. Overview of the study location and the Upper Rhine Graben. a) The study location is around 30 km east of the city of Karlsruhe in Knittlingen, isolines for the Heidelberg pull apart basin (red) and Rastatt trough outlining the depocenters (blue) (modified after Böcker et al., 2017; Busch et al., 2024; Gabriel et al., 2013; Schumacher, 2002). b) Marked location of the Upper Rhine Graben in blue box and Kraichgau area in SW Germany (modified after Busch et al., 2022b). Alpine deformation front (Alpine DF, dashed red line) adapted from Käßner et al. (2024). c) Simplified geological and tectonically map, the approximal location of the Knittlingen quarry is marked with a red star (redrawn and modified after Meier et al., 2015). d) Study location (red star) with paleogeographic distribution of landmasses during the middle Triassic Upper Muschelkalk (redrawn and modified after Franz et al., 2015; Warnecke and Aigner, 2019, and references therein). BG: Burgundy Gate, CG: East-Carpathian Gate, SMG: Silesian-Moravian Gate, LB: London Brabant Massif.

and Franz, 2005). The general evolution is described as subsidence and deposition from the Triassic to the Cretaceous, followed by uplift and erosion throughout the Cretaceous to Eocene. The remaining Mesozoic and newly deposited Cenozoic lithologies in the Upper Rhine Graben experience another phase of subsidence from the Eocene onwards (Bossennec et al., 2021 and references therein). In contrast to the Upper Rhine Graben, the Mesozoic lithologies on the graben shoulders did not experience an additional burial since the Eocene but were uplifted and are now exposed in outcrop. The present investigation is focused on rocks of the Knittlingen quarry. This study area is located on the eastern Upper Rhine Graben shoulder, approximately 30 km east of the city of Karlsruhe in Germany (Fig. 1a, b, c) where Middle Triassic Muschelkalk and Keuper lithologies (Early Anisian to Early Ladinian) are exposed.

The Upper Rhine Graben is a ca. 300 km long (Basel to Frankfurt/Main), and ca. 30–40 km wide intracontinental rift basin. It has an overall NNE-SSW strike direction (Fig. 1a), and was formed as part of the European Cenozoic Rift System (Schumacher, 2002; Ziegler, 1992). The region and location of the Upper Rhine Graben rift is linked to changing stress fields (Fig. 2) and reactivation of Permo-Carboniferous NNE-SSW oriented fault systems (Schumacher, 2002; Ziegler, 1992). During the Permian and Early Triassic, the region experienced N-S and NNE-SSW extension in a normal faulting regime (Dezayes and Lerouge, 2019).

For Central Europe, the σ_1-axis is reconstructed as NW-SE during the Early Cretaceous and NE-SW compression during the Late Cretaceous, persisting into the Paleocene (Kley and Voigt, 2008), leading to uplift in the area of the southern Germanic Basin (Böcker, 2015 and references therein) (Fig. 2).

During the Middle Eocene W-E directed extension resulted in reactivation of Permo-Carboniferous NNE-SSW oriented fault systems and initiated the Upper Rhine Graben rift formation (Schumacher, 2002; Ziegler, 1992). Subsequently, the maximum principal stress rotated clockwise towards a NNE-SSW oriented compression around the Middle to Late Eocene (Schumacher, 2002). In the late Eocene, extension and subsidence of the southern part of the graben occurred due to NNE trending Alpine compression (Rotstein and Schaming, 2011 and references therein).

During the Oligocene, rifting of the Upper Rhine Graben was characterized by W-E to WNW-ESE extension, leading to the development of NNE-SSW striking graben-parallel faults (Schumacher, 2002). The NNE-SSW striking faults are abundant in the Cenozoic sequence, whereas the NNW-SSE oriented faults mostly abut against these large faults (Reinhold et al., 2016).

Reorientation of the stress field during the Miocene resulted in a sinistral strike-slip movement along the boundary faults of the Upper Rhine Graben, leading to a direction of the maximum principal stress to NNW-SSE to NW-SE and development of minor faults with a predominant NNW-SSE strike (Schumacher, 2002). Consequently, NNE-SSW trending faults have been reactivated in the same shear direction (Ahorner, 1975; Schumacher, 2002).

The current stress field (principal stress directions and magnitudes) for the central region of the Upper Rhine Graben derived from well data from the Bruchsal geothermal site matches with σ_{Hmax} oriented approximately NW-SE (Meixner et al., 2014).

The continental Upper Rhine Graben rift basin accumulated Paleogene and Neogene marine and terrestrial deposits, which unconformably overly the Mesozoic sequence. Burial depths of Mesozoic units partly exceed 5000 m (Anders et al., 2013), related to pull-apart basins (Rastatt trough, south of Karlsruhe, Fig. 1a) forming in releasing bends. The structural configuration of the Upper Rhine Graben is characterized by intricate horst and graben formations, anticlines, monoclines, faulted anticlines and roll over-structures (Durst, 1991).

The Upper Rhine Graben is of primary focus for deep geothermal exploration in Central Europe, owing to high geothermal gradients exceeding 100 °C/km in certain areas, recorded for Tertiary, Jurassic and Upper Triassic (Keuper) sediments and sedimentary rocks from drill holes (Pribnow and Schellschmidt, 2000; Vidal et al., 2015), e.g., at the

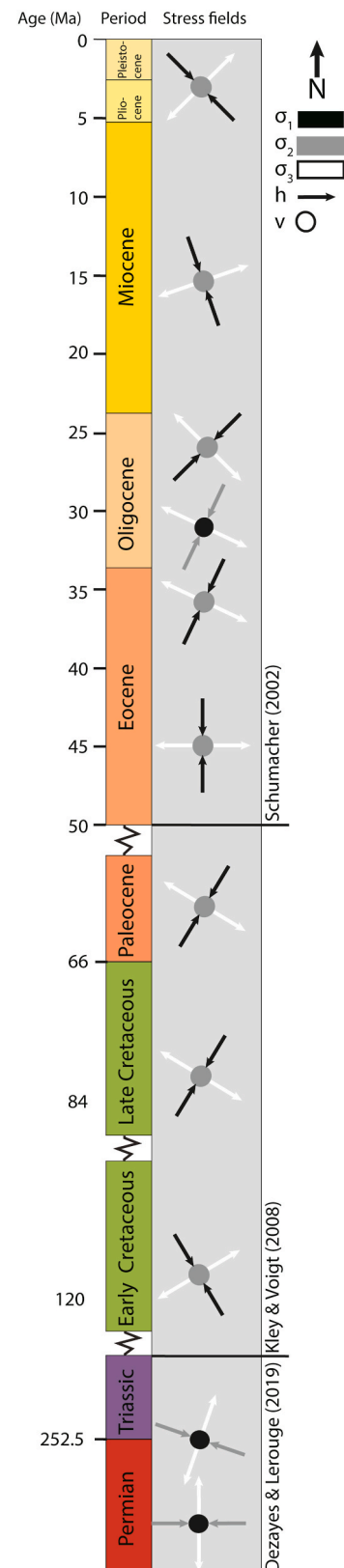**Fig. 2.** Changes in stress field over time in Central Europe. For the Permian and Triassic, a normal faulting regime with $\sigma_1 = \sigma_V$ is given (modified and redrawn from Dezayes and Lerouge, 2019). For Early Cretaceous to Late Eocene the stress field was dominantly compressional with $\sigma_1 = \sigma_{Hmax}$. Stress orientations are adapted from literature (modified and redrawn from Kley and Voigt, 2008; Schumacher, 2002).

Soultz-sous-Forêts site (Fig. 1a). High temperature gradients are generally related to conduction-dominated heat transfer, and low temperature gradients are indicative for convective fluid flow (Pribnow and Schellschmidt, 2000). Main fluid conduits are interpreted to be permeable fault damage zones and fractures, hosting convection cells in the Permo-Carboniferous basement and Permian to Middle Triassic sedimentary rocks (Vidal and Genter, 2018; Vidal et al., 2015).

3. Materials and methods

In the Knittlingen quarry a total of 32.3 m stacked vertical lithological profiles were recorded using the carbonate rock classification after Dunham (1962) to assess the depositional environment and link petrophysical measurements to lithotypes. The quarry has an overall north-south extension of ~440 m, a west-east extension of ~450 m while the main investigated southern part of the quarry has a north-south extension of ~275 m and a west-east extension of ~280 m. Measurements of spectral gamma ray (sGR) were conducted with a hand-held gamma ray spectrometer RS-230 BGO Super-SPEC detecting natural gamma radiation of ^{40}Th, ^{232}K and ^{238}U (cf. Schmidt et al., 2021). The measuring time was 60 s per spot with a distance of 20 cm between individual measurement spots. Measured sGR values were converted to API units using the following multipliers 1 ppm U = 8.09 API units, 1 ppm Th = 3.93 API units and 1 % K = 16.32 API units following Rider and Kennedy (2011). During lithological profile acquisition, individual limestone layers were sampled for petrophysical measurements and petrographic characterization. In addition, vein samples and samples of slickensides in the breached kink band planes were collected to assess their microstructure.

In total 109 plugs were drilled parallel (N = 45) and perpendicular (N = 64) to stratification using a water-cooled core drill with ~2.54 cm diameter (one-inch) from hand specimen for petrophysical analysis. Trim ends of individual plugs oriented parallel to the stratification were used for thin section preparation. The plugs were dried in a vacuum-oven until weight constancy at 40 °C for one week. Grain density and porosity were measured using a micrometrics AccuPycII 1340 pycnometer using helium (cf. Becker et al., 2017). Klinkenberg-corrected (Klinkenberg, 1941; Rieckmann, 1970) intrinsic permeability was measured with an air permeameter manufactured by Westphal Mechanic, with a measurement range between 0.0001 mD and 10,000 mD, using dry, oil-free laboratory air as permeant at a confining pressure of 1.2 MPa to avoid sample bypass under steady-state flow conditions (Busch et al., 2022a).

The assessment of permeability of undisturbed host rock samples and samples with partially sealed veins or stylolites at elevated confining pressures (30, 20, 10, 1.25 MPa) was assessed on three plug samples in an isostatic flow cell using helium as a permeant at room temperature (22 ± 1 °C) (cf. Monsees et al., 2020). Permeabilities were measured during the unloading cycle after all samples were loaded up to a maximum confining pressure of 30 MPa. The cell is fitted with a HPLC pump (high-performance liquid chromatography pump) using water to regulate confining pressures. As the results are apparent permeabilities, the Klinkenberg correction was used to correct possible slip flow (Amann-Hildenbrand et al., 2016; Klinkenberg, 1941). Pressure sensitivity coefficients of permeability (γ) were calculated after David et al. (1994) to compare the results. Since the reference effective confining pressure (P_0 in David et al. (1994)) is 1.25 MPa, the respective measurements at elevated confining pressures are plotted at 8.75, 18.75, and 28.75 MPa.

For petrographic analysis a total of 30 thin (~28 μm) and thick sections (100 μm) were prepared. All samples were embedded in blue dyed epoxy resin to visualize optical porosity. In total, 24 thin sections were stained on one half with a combined solution of alizarin red S and potassium ferricyanide to distinguish different carbonate phases after Dickson (1965) and covered with a glass cover slip. Dolomite remains unstained, whereas calcite will stain reddish (pink to orange), ferroan

calcite will stain blueish (purple to blue), and ferroan dolomite will stain pale blue (cf. Ölmez et al., 2024). Additionally, six samples were prepared as thick sections with a thickness of 100 μm and were polished for cathodoluminescence (CL) analysis. Furthermore, eight trim ends of plugs were fine ground with 4000 grit sand paper to assess fracture cements in CL.

For petrographic analysis a Leica DMLP fitted with a Progres Gryphax camera system was used, and polished thin sections were additionally examined using cold cathode cathodoluminescence (CITL CL8200 Mk5-2 Optical Cathodoluminescence System mounted on a Leica DIALUX 20 ES) in a vacuum to assess zonation or possible cross cutting relationships of individual vein and cement generations. Point counting was performed to link detrital or diagenetic cement phases to reservoir quality. Therefore, point counts were performed on 300 points on 24 thin sections using a Pelcon semi-automatic point count stage using a step-length of 250 μm to account for the variety of grain size (from micrite to mm sized shells) installed on a Leica DMLP microscope (as also shown in Busch et al., 2019). Optical porosity types were determined using the classification of Choquette and Pray (1970). As the grain size of micrite ($\leq$4 μm) and microsparite (5–10 μm) by Folk (1959, 1974) could not be determined during point-counting, the term micrite is used (cf. Ölmez et al., 2024). Grain size of dolomite was measured on the long axis of each crystal (at minimum 20 measurements per thin section) on microphotographs using ImageJ.

Drone image acquisition for orthomosaic generation to document the kink bands was performed using a DJI Phantom 4 Advanced Plus. The photogrammetric point-cloud and orthomosaic generation was done using Agisoft PhotoScan (now Metashape) (Allgaier et al., 2023b; Cawood et al., 2017). Fracture dip direction and dip angle were recorded using a manual compass (N = 576) and processed using OpenStereo (Grohmann and Campanha, 2010). We prepared two scan lines, recording fracture orientations once subperpendicular to the exposed breached kink band (striking NNW-SSE, 26.7 m length, N = 346) and once along a perpendicular wall (striking ENE-WSW, 11.88 m long, N = 133) in order to analyze fracture set intensities and clustering. Manual fracture detection (dip direction, dip angle) of the northern kink bands are based on point clouds in CloudCompare (Girardeau-Montaut, 2017) using the compass tool (e.g., see Allgaier et al., 2023b).

To assess fracture set intensities and gain information about spatial arrangement, we use the normalized correlation count (NCC) method (Marrett et al., 2018). This method distinguishes random fracture arrangements from clustered and periodic arrangements using the two-point correlation function or correlation sum (Bonnet et al., 2001; Wang et al., 2019). As fracture strike is not always perpendicular to the scan line, the recorded apparent distances between the fractures require correction using the Terzaghi method (Li et al., 2018; Terzaghi, 1965). For this purpose, sub-parallel sets of five main fracture strike orientations were grouped into sets (striking 10°, 50°, 70°, 110°, 140°), resulting in corresponding 338 fractures in total for these analyses. The sets were differentiated based on strike rose and polar plot density clusters. The respective angle between the strike of the fracture set and the scan line was used to obtain corrected distances (Li et al., 2018; Terzaghi, 1965). The generated data was analyzed using CorrCount in Matlab (cf. Marrett et al., 2018). Pattern morphology of normalized correlation counts were described after Marrett et al. (2018) and Li et al. (2018), as either indistinguishable from random, anti-clustered individuals, regularly-spaced individuals, regularly-spaced fractal clusters, clustered individuals, fractal cluster or log-periodic cluster (Marrett et al., 2018, their Fig. 12). As no bedding planes were accessible in the quarry, no data on fracture length and connectivity can be obtained.

To assess the relation of present fracture orientations and present-day stress orientation, we also performed dilation and slip tendency analyses (Allgaier et al., 2023b; Ferrill et al., 2020; Morris et al., 1996) in FracTend (Healy, 2023). Dilation and shear tendency analyses identifies fractures in which the ratio of shear stress (τ) to effective normal stress (σ_n) exceeds the frictional strength (μ) of the fracture, they are therefore

critically stressed and show a higher probability of being hydraulically conductive (Barton et al., 1995; Ferrill et al., 2020). The slip tendency T_s (Eq. (1)) reflects the likelihood of fracture reactivation in shear mode assuming no cohesion (Morris et al., 1996) and the dilation tendency T_d (Eq. (2)) reflects the likelihood of a plane to dilate (to open) in tensile mode (Ferrill et al., 1999):

$$T_s = \frac{\tau}{\sigma_n} \geq \mu \qquad\qquad\qquad\qquad \text{Eq. 1}$$

$$T_d = \frac{(\sigma_1 - \sigma_n)}{(\sigma_1 - \sigma_3)} \qquad\qquad\qquad\qquad \text{Eq. 2}$$

Using the trend and plunge of the poles of recorded fractures from the two scanlines and the reconstructed present-day stress orientation and magnitude in the Upper Rhine Graben (Allgaier et al., 2023a; Meixner et al., 2014) at 1000 m depth using stress gradients $\sigma_2 = \sigma_V = 23.8$ MPa/km, $\sigma_1 = \sigma_{Hmax} = 28.8$ MPa/km, $\sigma_3 = \sigma_{hmin} = 15.3$ MPa/km and pore pressure of 10.2 MPa/km allows the assessment which fracture orientations are more likely to contribute to fluid flow.

4. Results

4.1. Lithological description and gamma ray signature

4.1.1. Overview
The Knittlingen quarry exposes Upper Muschelkalk to Lower Keuper lithologies, fractures, veins and faults. In both quarry parts (northern and southern part, Fig. 3a), kink bands are present, and in one wall a breached kink band with mineralization is exposed. This study focuses on the southern part of the quarry (red box in Fig. 3a). In the studied area (Fig. 3b) stacked vertical lithological profiles were recorded (red lines in Fig. 3b–d). Manual compass measurements were taken along the lithological profiles, and on scan lines (orange lines in Fig. 3b).

4.1.2. Upper Muschelkalk
In total, 25.8 m of limestone – marly claystone alternations for the Upper Muschelkalk is recorded (Figs. 4 and 6). The Upper Muschelkalk lithologies are composed of dark grey to very dark grey, mostly calcitic, mudstones, wackestones, and packstones (further called limestones) classified after Dunham (1962) and very dark grey marly claystone intercalations (Figs. 4 and 6).

The number of intercalated marly claystones decreases toward the top of the studied lithology (Fig. 4a and b). The recorded wacke- or packstones include (recrystallized) shell fragments (Fig. 4b), showing a dark grey or white color. Some of the shells are non-reactive to HCl indicating a dolomitic or silicic composition. The limestone texture is mostly massive. Toward the younger strata, wacke- and packstones are more abundant than mudstones (Fig. 4a (older strata), b (younger strata), 6). Subordinately, erosional surfaces and bioturbation between underlying mudstones and overlying wacke-/packstones can be observed (Fig. 4c and d). Both, decreasing marly claystone contents and the increasing amount of shells within the limestones indicate a general shallowing upward trend. Calcitic veins (mm-thick) are present perpendicular to bedding, mostly strata-bound and rarely crosscutting multiple limestone beds.

4.1.3. Lower Keuper
For the Lower Keuper, a total of 6.5 m of limestone – marly claystone alternation is recorded. The limestones are mostly massive mudstones. At the base of a dark grey marly claystone layer (Vitriolschiefer), an approximately 2 cm thick bonebed layer can be found (Fig. 5a). This is followed by a thicker limestone layer (Blaubank) with brachiopod impressions, bioturbation, and cavities at the base indicating dissolution (Fig. 5b). Toward younger strata, the claystone content increases and only thinner calcitic limestone beds are exposed (Figs. 5c and 6).

4.1.4. Lithological column and spectral gamma ray (sGR)
The calculated sGR for the Upper Muschelkalk profiles (N = 135) varies between 16 and 86 API and generally decreases from the base of the studied Upper Muschelkalk section toward the top, reflecting the recorded decrease in marly claystone layers throughout the lithological column (Fig. 6). The calculated sGR for the Lower Keuper profiles (N = 30) ranges from 48 to 151 API (Fig. 6). The base of the Keuper is indicated by increasing gamma ray values, related to the sudden increase in marly claystone content.

4.2. Petrography

The stained thin sections confirm the macroscopic classification as limestones. A detailed point-count table is found in supplementary materials I and all contents are given as vol% of the bulk sample. As most of the point-counted thin sections are limestones from the Upper Muschelkalk and only one is from the Lower Keuper, samples are not classified based on their stratigraphy. The fine-grained, calcitic, matrix is summarized as micrite.

4.2.1. Detrital components
The samples are dominantly composed of calcitic micrite (crystal sizes between <4 and ~13 μm), biodetritus (e.g., shells, crinoids, gastropods, teeth, or fish scales), or peloids. The most abundant detrital components are micrite (Fig. 7a), ranging from 0 to 93 %, peloids (Fig. 7a, 0–21.7 %) which are distributed without any orientation and mostly composed of calcitic micrite, and crinoid fragments (0–6.7 %). Intercrystalline clay between dolomite spar (0–6.0 %) is present in three samples. Phosphatic peloids, bone fragments, scales, and teeth are summarized as phosphates (0–1.3 %) and occur in most of the samples (Fig. 7f), but were not always encountered during point counting. Individual samples show mostly undeformed ooids (up to 12 %, Fig. 7c) with mostly bioclastic centers. Quartz grains (0–0.3 %) occur rarely, whereas shell fragments showing primary textures and calcitic composition (0–9.3 %) are present in most of the samples. Gastropods (0–0.3 %) were observed in different samples, but were only point counted twice. Ostracods (0–4.7 %) are only encountered in one sample, but are highly concentrated in individual layers (Fig. 7d).

4.2.2. Authigenic components
The main authigenic phases are calcite spar (0–48.7 %, Fig. 7c) that occurs distributed in the samples, replacive chert in shell fragments (0–41.0 %), and neomorphic replacements of shells with calcite spar (0–31.3 %, Fig. 7f) growing from the rim into the center of the shell. Micritic envelopes are mostly seen on recrystallized shells and only subordinately on crinoid fragments, and make up between 0 and 19.7 % (Fig. 7e). Some of the recrystallized shells additionally show both, the replacement with calcite spar at the shell rim, and Fe-calcite in the center (Fig. 7f), the latter ranging between 0 and 15.0 %. Individual shells are additionally replaced by not only chert but also macrocrystalline quartz (0–9.3 %). Where chert replaces bioclasts, it often transitions into macrocrystalline quartz, which is again encased in Fe-calcite replacements of bioclasts (Fig. 7l). Individual shells also show additional replacement by dolomite (Dol, 0–10.0 %), of which some additionally show a Fe-dolomite (Fe-Dol) rim (0–2.0 %) (Fig. 7k). Dolomite and Fe-dolomite replacements often show curved crystal facets, pleochroism, and undulose extinction, typical of saddle dolomite. Dolomite spar (Fig. 7c–e) also replaces peloids and ooids in individual samples (0–21.7 %), as well as micrite (0–31.3 %, Fig. 7b) mostly as planar-e to planar-s rhombs, where few of the dolomite spars also show a Fe-dolomite rim (0–3.0 %). These dolomite rhombs show almost no pleochroism in plane-polarized light. In some samples, only the peloidal shape remains, whereas the detritus is fully dolomitized. Where dolomite spar in e.g., bioclasts is (partially) dissolved, FeO/FeOOH outlines (0–4.3 %) are often observed. Because of different optical properties of the dolomite, the crystal size was additionally measured, to distinguish
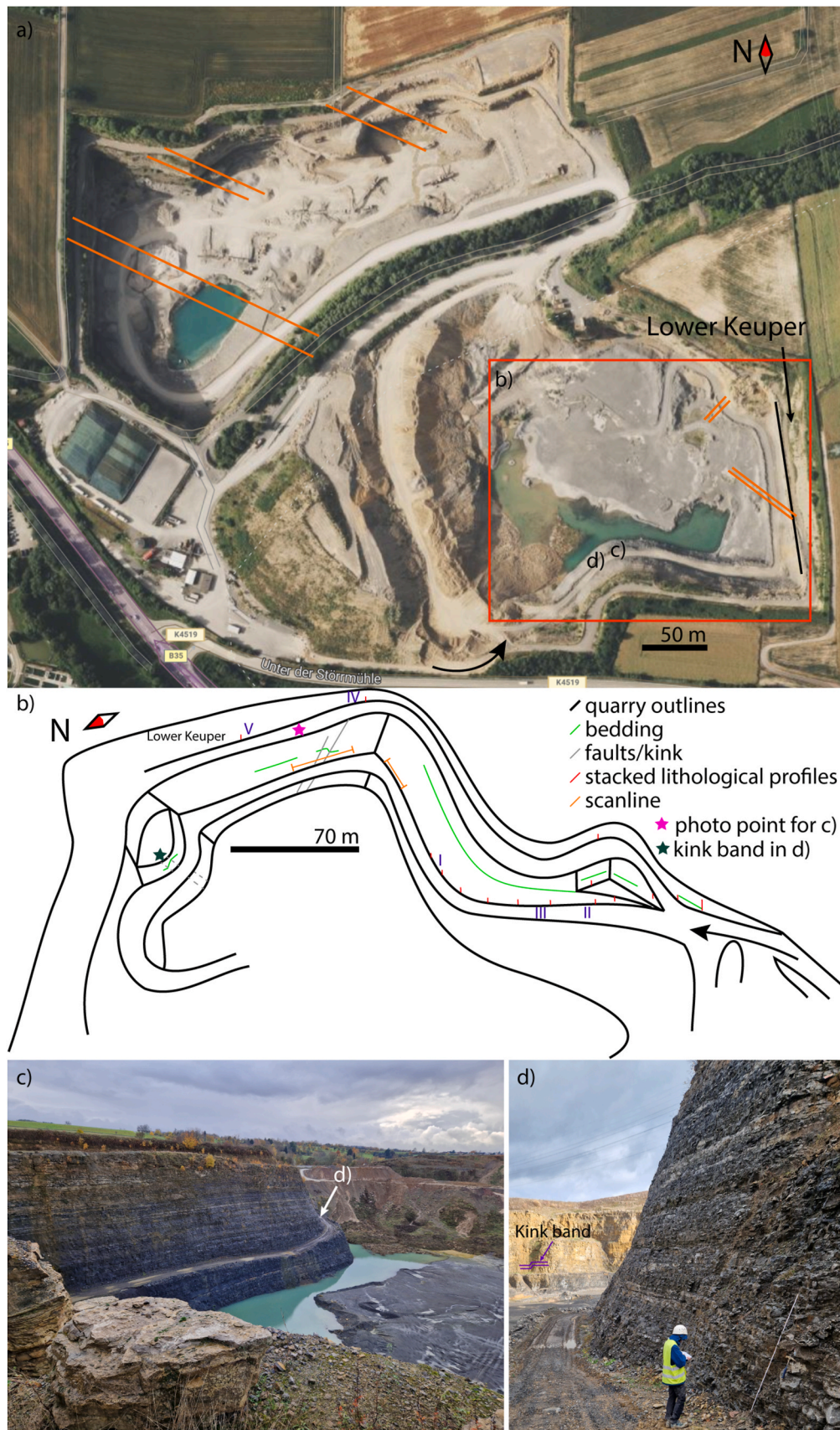
Fig. 3. Overview of the quarry. a) Aerial image of the quarry, the NE part is currently mined, the study location is marked with a red box and redrawn as schematic map in b). Orange lines indicate location and strike of kink band planes (Bing maps, 2025). b) Schematic map of the study area and locations of sampling and stacked vertical lithology descriptions (red lines), roman numbers are shown in Fig. 4 (I, II, III) and 5 (IV and V). c) View from top into the quarry, where Upper Muschelkalk lithologies are exposed. d) Record of vertically stacked lithologies profiles, and one kink band in the background, location is marked with a dark green star in b).
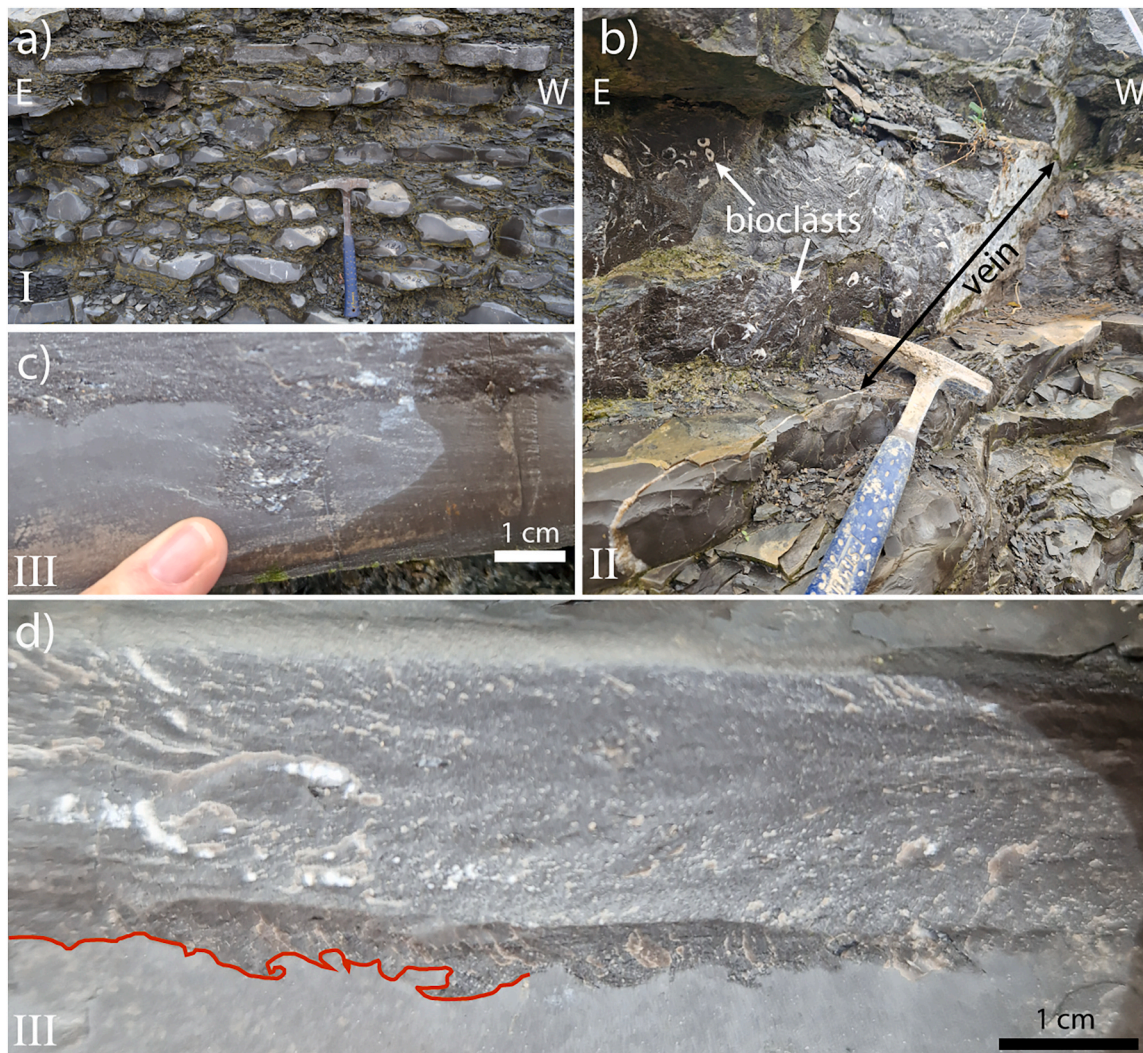
Fig. 4. Overview of the Upper Muschelkalk, locations in the quarry are marked in Fig. 3b as roman numbers. a) Lower part of the studied succession with more marly claystone interbeds. b) Upper Muschelkalk, alternation of marly claystones, mudstones and packstones with bioclasts (bivalves and brachiopods), and a calcite vein penetrating several banks. c) Upper Muschelkalk, bioturbation trace, maybe glossifungites or similar. d) Upper Muschelkalk, erosion (some parts outlined in red) of underlying mudstone.

three dolomite types:

- Dolomite type I crystals (Fig. 7c), observed as fabric-selective dolomitization of ooids/peloids (almost no pleochroism, dusty appearance, normal extinction) with crystal sizes from 0.03 to 0.30 mm (avg.: 0.11 mm).
- Dolomite type II crystals (Fig. 7b), replacing the matrix (no pleochroism, dusty appearance in the center) with smaller crystal sizes from 0.01 to 0.14 mm (avg.: 0.05 mm), often associated to intercrystalline clay minerals.
- Dolomite type III crystals (Fig. 7i–k) replacing bioclasts, matrix and vein cements (strong pleochroism, dusty appearance, undulose extinction) with larger crystal sizes from 0.04 to 1.30 mm (avg.: 0.27 mm).

Detrital components show an isopachous fibrous to bladed radial calcitic rim cement (0–31.7 %) which is the dominant cement in two samples (Fig. 7c, e), and is less frequent in samples containing higher micritic matrix contents. Additionally, one sample also shows parts of calcitic rim cements replaced by SiO_2 (0.7 %), where the detrital component is also (partly) replaced by chert. Pore filling cements are Fe-calcite (0–10.3 %), dolomite (0–2.3 %), and chert (0–1.3 %), which are

observed in between biodetritus, occasionally also encasing rim cements where present (Fig. 7c). Pyrite (0–7.0 %) is present within the majority of the samples, and mostly present in the matrix and in bioclasts, and rarely occurs as geopetal pyrite in bioclasts in individual samples. Additionally, pyrite is also present in one sample at the interface between the host rock and a composite dolomite and Fe-calcite vein. One sample shows a druse, which is filled by chert, which transitions into macro quartz, and some of the remaining pore space is filled with calcite and/or Fe-calcite, with some areas of the thin section showing non-pervasive quartz pseudomorphs after sulphates (up to 4.3 %, Fig. 7g), indicated by bladed crystal morphologies filled by quartz. Additionally, one sample with a larger recrystallized shell also shows quartz pseudomorphs after sulphate evaporites (0.7 %). Authigenic quartz is present as laths with euhedral outlines within the matrix (Fig. 7c), containing solid inclusions of the replaced material, in some thin sections, but where only point counted once (0.3 %).

Clay mineral-rich stylolites are not always encountered during point-counting and vary between 0 and 4.3 %. In one sample, the stylolite shows defined sutured boundaries (Fig. 7i), whereas this effect is less pronounced in other samples (Fig. 7j). Stylolites are characterized by enrichment of e.g., clay minerals along pressure dissolution fronts. The columnar side of the stylolites show thinner clay mineral accumulations.
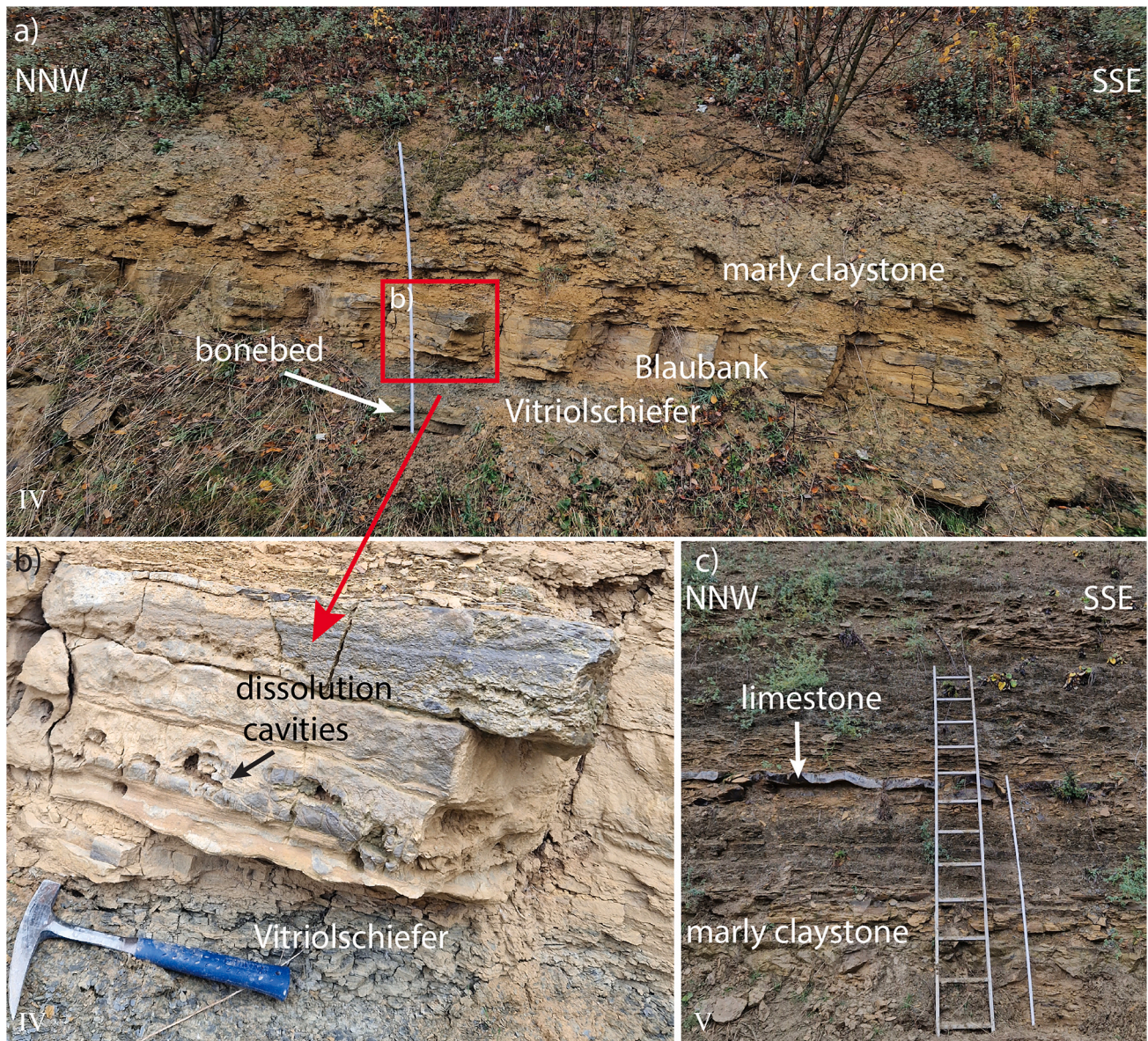
Fig. 5. Overview of the Lower Keuper, locations in the quarry are marked in Fig. 2 as roman numbers. a) Succession of bonebed containing fish teeth, phosphatic pellets, bone fragments, ostracods and dark grey Vitriolschiefer, Blaubank and marly claystone. b) The calcitic Blaubank show layer of ostracods and dissolution cavities. c) The topmost studied section is dominantly composed of marly claystone and only thinner limestone beds (mudstones) occur.

Some stylolites are associated to veins and displace them (Fig. 7j). Wispy, discontinuous dissolution seams, not yet forming a stylolite (i.e. lacking the columnar features), were not encountered during point counting, but are present in individual samples.

Vein cements are of calcitic composition (0–10.7 %), Fe-calcite (0–17.7 %) or occur as veins showing internal zonation of these. Dolomite vein cements (0–7.0 %) show pleochroism and undulose extinction typical for saddle dolomite, which is on occasion encased by Fe-calcite and subordinately Fe-dolomite (0.3 %).

4.2.3. Optical porosity

Optical porosity was differentiated into intraparticle porosity (0–14.7 %), fracture porosity (0–2.0 %) in partially sealed veins, and in one sample mouldic porosity (0.3 %). Intraparticle porosity is mostly restricted to areas where bioclasts are dissolved or replaced, e.g., in dolomitized peloids or ooids.

4.2.4. Cathodoluminescence

Cathodoluminescence (CL) analyses were performed to gain additional insight into the structural and diagenetic development based on characteristic luminescence behavior of components and cements. Furthermore, CL analyses may allow a more detailed assessment of fracture cement paragenesis, based on cross-cutting relationships. Slight differences in luminescence intensity between samples are due to different surface qualities of polished thin sections and fine ground trim ends.

In the studied samples calcite mostly shows an orange luminescence, Fe-calcite and Fe-dolomite are dull to non-luminescent and dolomite shows a purple-reddish luminescence (Fig. 8a). Veins or recrystallized shells often show internal sector zoning of calcite and Fe-calcite and are combined as (Fe-)calcite cements (Fig. 8b).

Some veins show partially sealing cements with sector zoned crystals bridging the fracture (Fig. 8c), other veins are pervasively sealed and cross-cut and displaced by a younger vein generation. Individual micritic peloids cannot be accurately distinguished from cements or
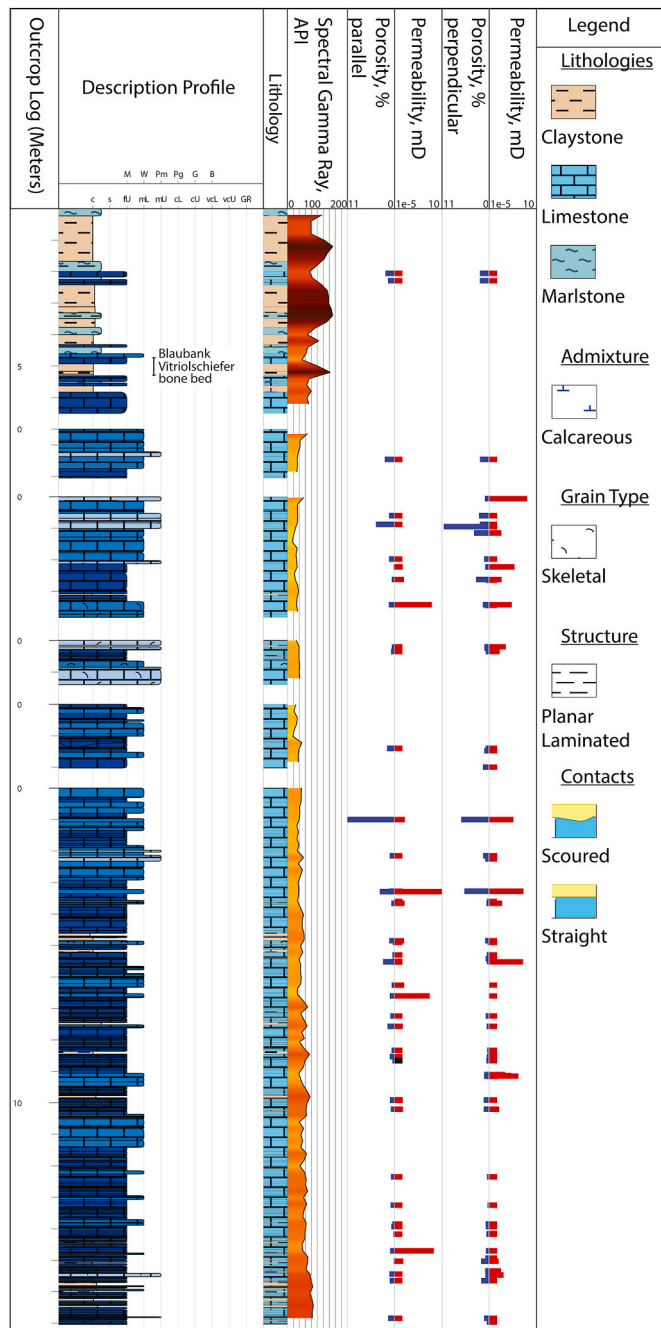
Fig. 6. Lithological column of stacked vertical logs from topmost Lower Keuper (6.5 m in total) to Upper Muschelkalk (25.8 m in total), sGR in API, helium porosity (%, blue) and permeability (mD, red) of plug samples from limestone beds drilled parallel or perpendicular to bedding.

micrite forming the matrix based on different luminescence colors. Crystal boundaries or the boundary between peloid/ooid and the rim cement only occasionally show a slightly brighter luminescence (Fig. 8c). In individual samples larger shells are also overgrown by saddle dolomite with reddish-purple luminescence and a non-luminescent Fe-dolomite rim, encased by (Fe-)calcite (Fig. 8d).

4.2.5. Relation of fracture cementation

In addition to cathodoluminescence analyses on host rocks, three vein samples and two samples of the cemented slickensides from the breached kink band were studied. Partially fracture filling saddle dolomite shows a reddish-purple luminescence and pyrite at the host rock-

vein interface (1, Fig. 9a and b). This vein also includes (Fe-)calcite cements encasing euhedral dolomite crystal facets (2, Fig. 9b). This composite vein is crosscut by a dull to non-luminescent (Fe-)calcite vein (3, Fig. 9a and b). These mostly pervasively sealed blocky (Fe-)calcite veins show weak internal sector zoning in dull orange luminescing cements in CL analyses (3, Fig. 9c). These are crosscut by a brighter (Fe-)calcite vein, showing internal sector zoning in bright and dull orange luminescing cements (4, Fig. 9c). A vein generation composed of mostly dull luminescing Fe-calcite cement, which in some samples shows slightly brighter luminescence, is only found in a sample from the fault zone (5, Fig. 9g) and is crosscut by brighter cement phases (6, 7, Fig. 9g). One of those brighter vein cements is also only found in samples from the fault area and shows a heterogeneous luminescence without distinct zoning (6, Fig. 9f and g). A partially fracture-filling (Fe-)calcite phase showing internal zonation of more dull or bright zones and euhedral crystal facets is observed (7, Fig. 9d, f, h). This vein phase is crosscut other vein cement generations if present in host rock and fault samples. This zoned luminescence cement phase (7) is additionally enclosed by a dull-non-luminescent Fe-calcite phase forming the rim of a partially sealed vein in the fault core (8, Fig. 9h). Additionally, some veins include host rock inclusions in both host rock samples and fault samples, which are in some cases arranged parallel to the host rock-vein interface (Fig. 9d), and imply fracturing following initial fracture cementation.
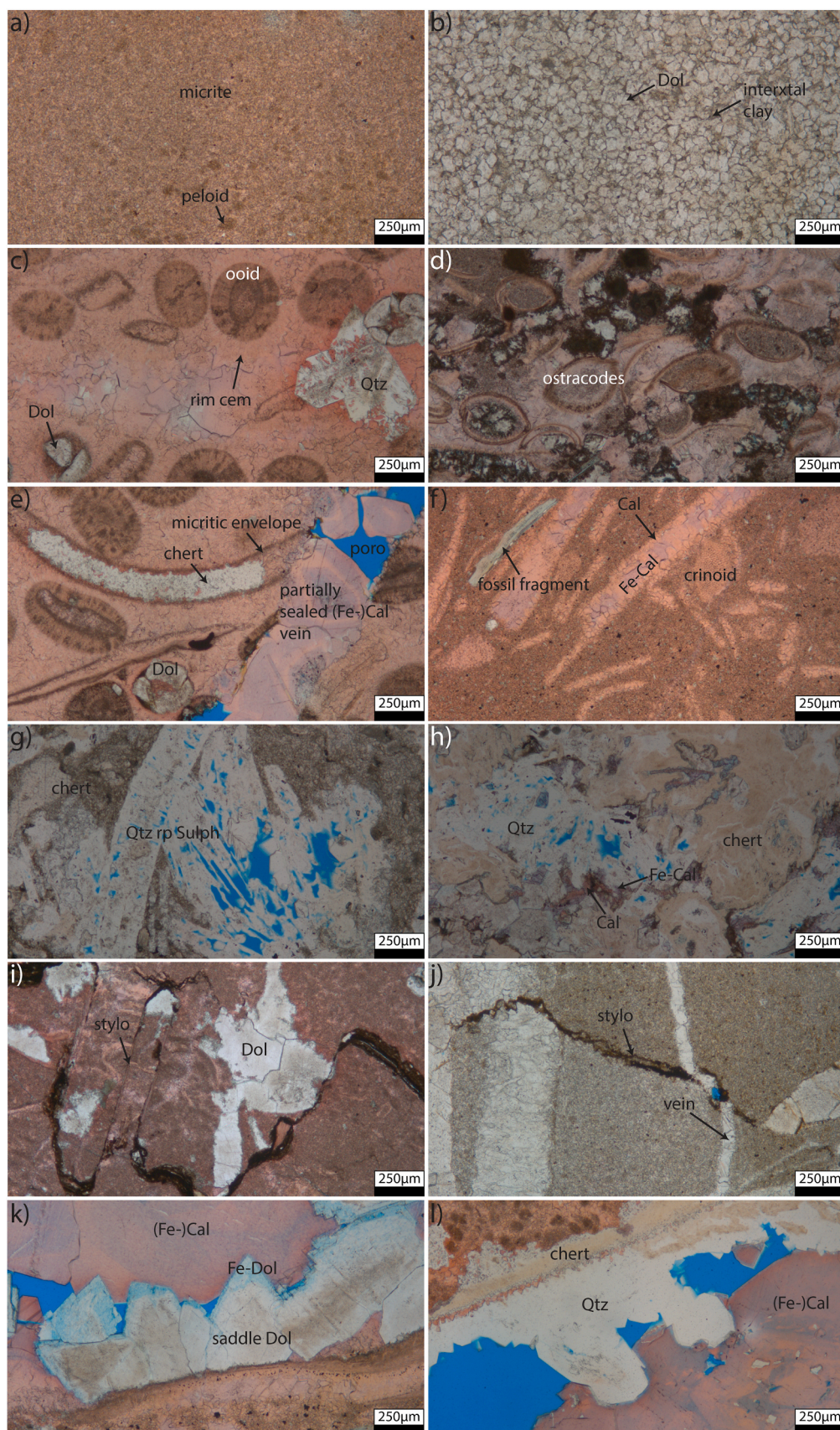
4.3. Porosity, permeability and density

For Muschelkalk samples drilled parallel to stratification, He-porosity ranges between 0.13 and 10.87 % (avg.: 1.33 %), grain density ranges between 2.68 and 2.73 g/cm^3 (avg.: 2.73 g/cm^3), and bulk density ranges between 2.41 and 2.72 g/cm^3 (avg.: 2.67 g/cm^3), while the permeability ranges between <0.0001 mD and 9.7 mD (avg.: 0.27 mD). Two Keuper samples show He-porosity of 1.53 % and 2.13 %, permeabilities of <0.0001 mD, grain density for both of 2.7 g/cm^3 and bulk density of 2.65 g/cm^3 and 2.66 g/cm^3.

The measured He-porosities for Upper Muschelkalk samples drilled perpendicular to bedding range from 0.16 to 10.58 % (avg.: 1.33 %), while grain density ranges from 2.67 to 2.75 g/cm^3 (avg.: 2.71 g/cm^3), and bulk density ranges from 2.44 to 2.74 g/cm^3 (avg.: 2.67 g/cm^3). Gas permeability varies between <0.0001 mD and 0.6283 mD (avg.: 0.0186 mD). He-porosity for two Keuper samples are 2.16 and 2.18 %, permeability is < 0.0001 mD, grain density is 2.69 g/cm^3 and 2.70 g/cm^3, and bulk density is 2.63 g/cm^3 and 2.64 g/cm^3. The highest porosity values are measured in samples showing druses.

Due to the measurement limit of the device, samples measured below the limit are given as 0.0001 mD for further rock typing. He-porosity and gas permeability show no correlation (Fig. 10a). Rock types (mudstone, wackestones, and packstone) show no correlation with porosity or permeability (Fig. 10b). The highest permeability is measured in samples showing either veins and stylolites or partially sealed veins (Fig. 10b).

Three samples were additionally measured under elevated confining stress (Fig. 11). Sample I contains a partially sealed vein, axially crossing the whole plug, sample II contains stylolites parallel to stratification and the axis of the plug, and sample III is a host rock sample without any special features and is described as a massive wackestone (Fig. 11). At 30 MPa confining pressure permeabilities are 0.13 mD for sample I, 0.05 mD for sample II and 3.0*10^{-6} mD for sample III. At 1.25 MPa confining pressure, permeabilities are 0.32 mD for sample I, 0.27 mD for sample II and 2.7*10^{-5} mD for sample III. The calculated pressure sensitivity coefficients of permeability γ are 0.03 for sample I, 0.06 for sample II and 0.071 MPa^{-1} for sample III (supplementary material I) and are at lowest for the sample containing the partially sealed vein. When normalizing the permeability measurements to the highest measured value of each sample (1.0), the sample containing the partially sealed vein retains 41 % of the initial permeability, whereas the sample containing the stylolite only retains 16 % and the undisturbed host rock only

(caption on next page)

Fig. 7. Photomicrographs of detrital components and authigenic phases of Upper Muschelkalk and one Keuper sample. a) Calcitic micrite and micritic peloids. b) Sparitic dolomite (planar-s) with cloudy centers, clear rims and intercrystalline clay (interxtal clay) between the spars. c) Calcitic ooids of which some are replaced by dolomite spar show a calcitic isopachous fibrous rim cement and authigenic quartz laths. d) Keuper sample, ostracods are aligned parallel to bedding, dolomite spars are distributed between bioclasts and calcite spar cements or in bioclasts. e) Partially sealed vein with internal zonation of ferroan calcite and calcite, one shell fragment is replaced by chert, ooids are either dolomitized or not and one show one dolomite rhomb in the ooid rim. f) Shell fragments with elongate blocky to euhedral calcite cement, and sparitic Fe-calcite (Fe-Cal) cement in the center, and a calcitic crinoid fragment. g) In former shells, chert and replacive quartz are abundant, in some areas overgrown by macroquartz (h), and some of the remaining porosity is filled with calcite or ferroan calcite. i) Columnar stylolites and dolomite cement. j) Stylolite displaces a vein (unstained section). k) Saddle dolomite overgrown a shell shows a ferroan dolomite rim and is encased in ferroan calcite and calcite. l) Macroquartz overgrows chert and is encased by ferroan calcite and calcite.
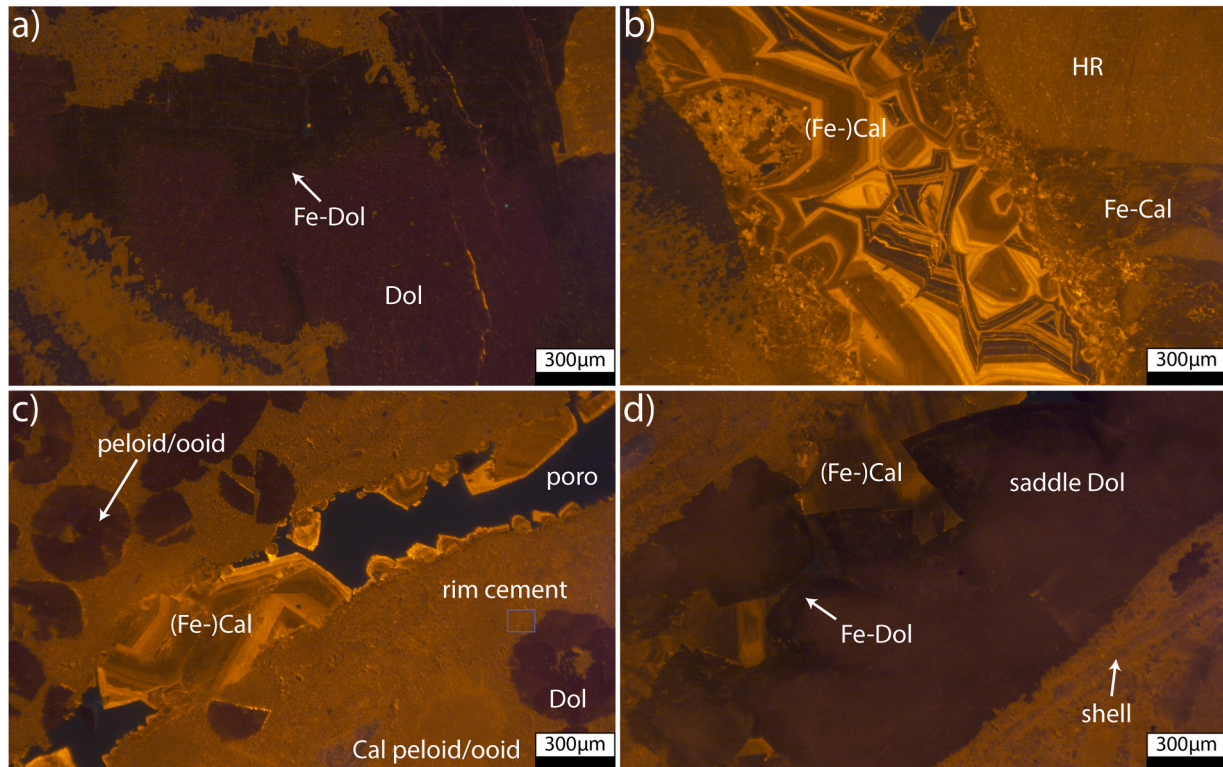

Fig. 8. Cathodoluminescence on thin sections and plug trim ends. a) Reddish-purple luminescence of dolomite and non-luminescence Fe-dolomite rim with surrounding calcite spar with orange luminescence and some calcite spar with dolomite cementer (M15). b) Euhedral (Fe)calcite crystal facets with internal zonation of calcite and non-luminescent Fe-calcite in a vein (M15). c) Dolomitized former ooids or peloids with purple luminescence, whereas calcitic ooids/peloids with calcitic rim cements (blue box) show (dull) orange luminesce, but not as bright as calcitic zones in the vein (M16). Partially sealed (Fe)calcite vein with bridging crystals. d) Larger shell replaced by saddle dolomite with Fe-dolomite rim and (Fe)calcite (M43).

retains 11 % of the initial permeability at 1.25 MPa confining pressure.

4.4. Rock typing

Rock typing links the porosity and permeability measurements with petrographic properties and enables the assessment of reservoir quality controls (Fig. 12). As not every plug has a corresponding thin section, the plots only represent a part of the petrophysical measured samples shown in Fig. 10. The micrite content does not correlate to differences in reservoir quality (Fig. 12a), only one sample with comparatively higher amount of micrite shows higher permeability but not enhanced porosity. The content of shells (with primary features) and recrystallized shells does not correlate to enhanced porosity or permeability (Fig. 12b), since samples with shell contents between 20 and 30 % show among the lowest and highest permeabilities. The fracture porosity and vein cements (Fig. 12c) and stylolite content (Fig. 12d) appear to affect permeability of individual samples, since individual samples with higher permeability show higher stylolite contents or preserved fracture porosity in partially cemented veins. Where veins are pervasively sealed, permeability remains low (~0.0001 mD). One sample displaying a stylolite which is oriented parallel to the plug's long axis and bedding

enhances the fluid flow at 1.2 MPa confining pressure (Fig. 12d, blue square).

Our study established that the matrix permeability of the studied limestones is low (max. 9.7 mD for one sample with a partially sealed vein and parallel to the measurement direction, else max. ~1 mD). Fractures and partially sealed veins enhance permeability if they have a suitable orientation parallel to measurement direction (Figs. 10–12). Hence, reservoir quality seems to be mostly related to structural elements in the studied lithology.

4.5. Structures and fractures

Fractures recorded along the lithological column and the two scanlines (N = 576) show three main strike orientations (NNE-SSW, WNW-ESE, NW-SE) and subordinate sets (NE-SW, ENE-WSW, W-E and NNW-SSE) (Fig. 13). The highest frequency is observed in WNW-ESE and NNE-SSW orientations.

Several decameter-scale reverse kink bands are exposed in the southern (Figs. 3a and 14a-c) and northern quarry parts (Figs. 3 and 14d). While the four kink bands in the northern quarry part consistently dip toward 021°–034° with dips ranging from 49° to 67° (Fig. 15, blue
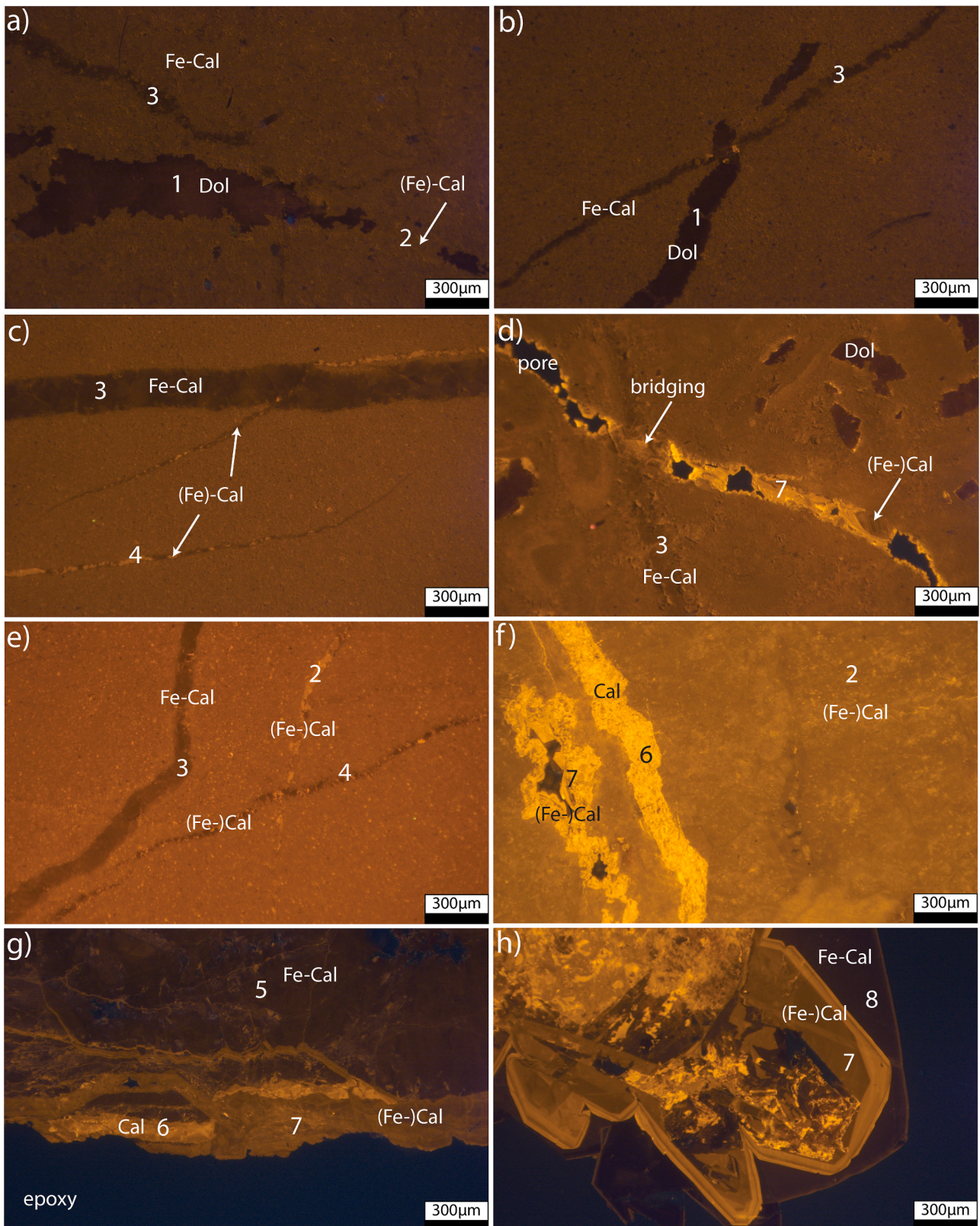
Fig. 9. Cathodoluminescence on vein thin sections from host rocks and fault area. a), b) Dolomite vein show some patches of (Fe-)calcite cement and is crosscut by a Fe-calcite vein (M25). c) Dull to non-luminescent Fe-calcite vein is crosscut by a (Fe-)calcite vein with internal zonation (M27). d) Partially sealed (Fe-)calcite vein with bridging crystals and internal zonation. Dolomite in ooids/peloids show reddish-purple luminescence (M14). e) Darker and brighter Fe-calcite veins are crosscut by a darker, partially non-luminescent (Fe-)calcite vein (KB_vein). f) Perversely sealed bright vein crosscut a darker luminescent (Fe-)calcite vein. A younger phase shows remaining pore space and cementation with (Fe-)calcite and euhedral crystals (KB_FL). g) Non-luminescent Fe-calcite vein and a brighter cement phase with is displayed by a (Fe-)calcite phase (KB_VB). e) Larger euhedral (Fe-)calcite and Fe-calcite cement in partially sealed vein (KB_FL).
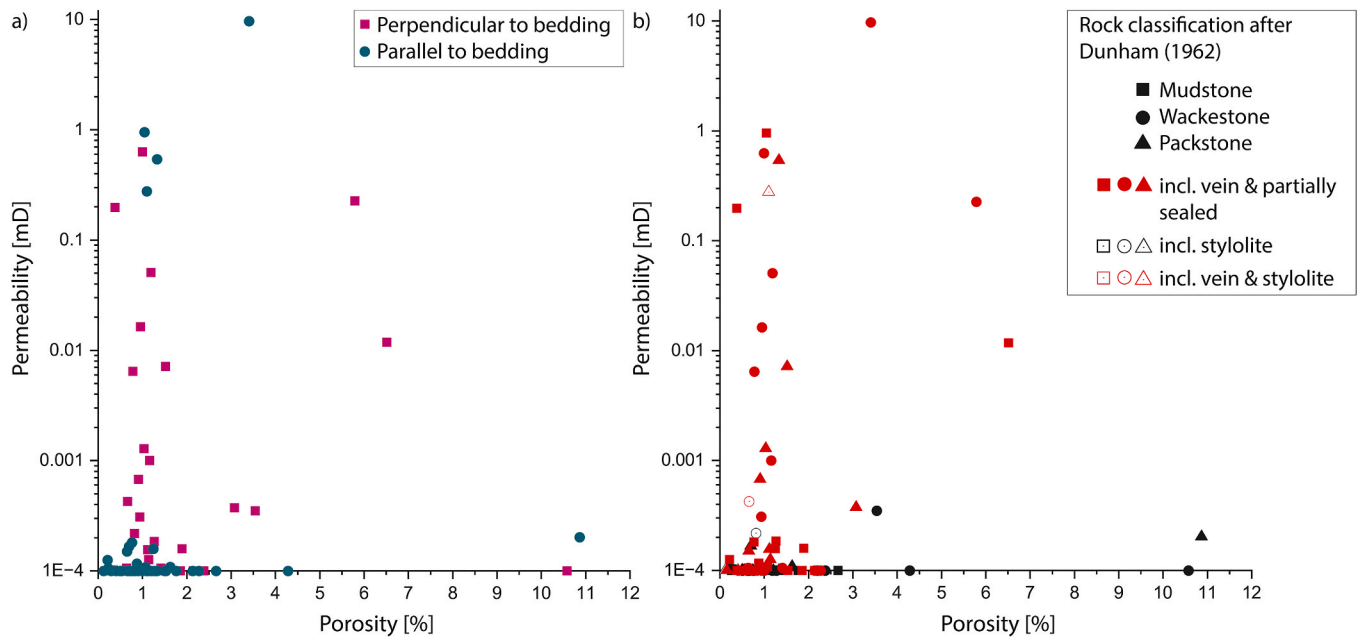
Fig. 10. He-porosity and gas permeability plots. a) Porosity and permeability show no correlation; green dots are samples drilled parallel to bedding and purple squares are samples drilled perpendicular to bedding. b) Rock type after Dunham (1962) (shape of symbols) show no correlation with porosity and permeability. Only samples which include either (partially sealed) veins or stylolites, or both, can enhance the permeability. The samples showing the highest permeability value shows a fracture oriented parallel to measurement direction, which is only marginal sealed and thus enhances the fluid flow in measurement direction. Samples with stylolites are shown as unfilled symbols with black outline, samples with (partially sealed) vein and stylolite are displayed as unfilled symbols with red outline.
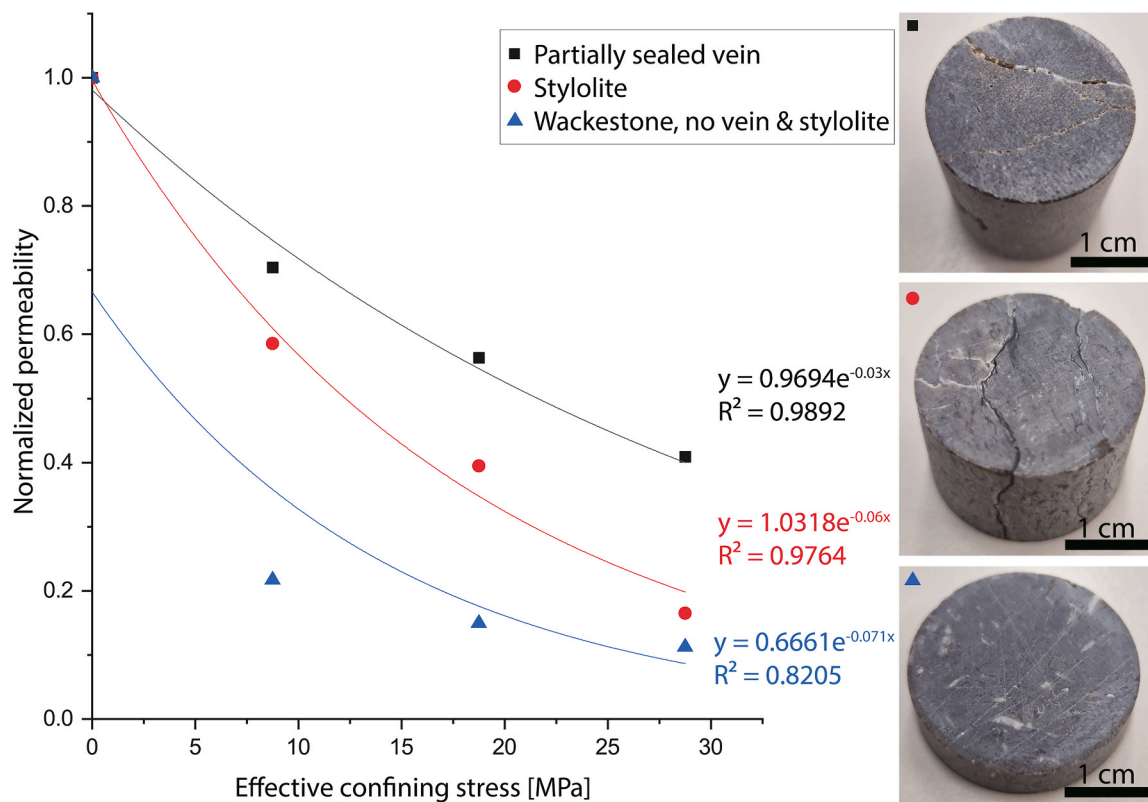

$$y = 0.9694e^{-0.03x}$$
$$R^2 = 0.9892$$

$$y = 1.0318e^{-0.06x}$$
$$R^2 = 0.9764$$

$$y = 0.6661e^{-0.071x}$$
$$R^2 = 0.8205$$

Fig. 11. Normalized permeability measured with decreasing effective confining pressures of 30 to 1.25 MPa and exponential trend lines. The permeabilities are normalized to initial permeabilities measured at 1.25 MPa. Thus, the permeability of a partially sealed vein sample at 30 MPa is c. 41 % lower than the permeability at 1.25 MPa.
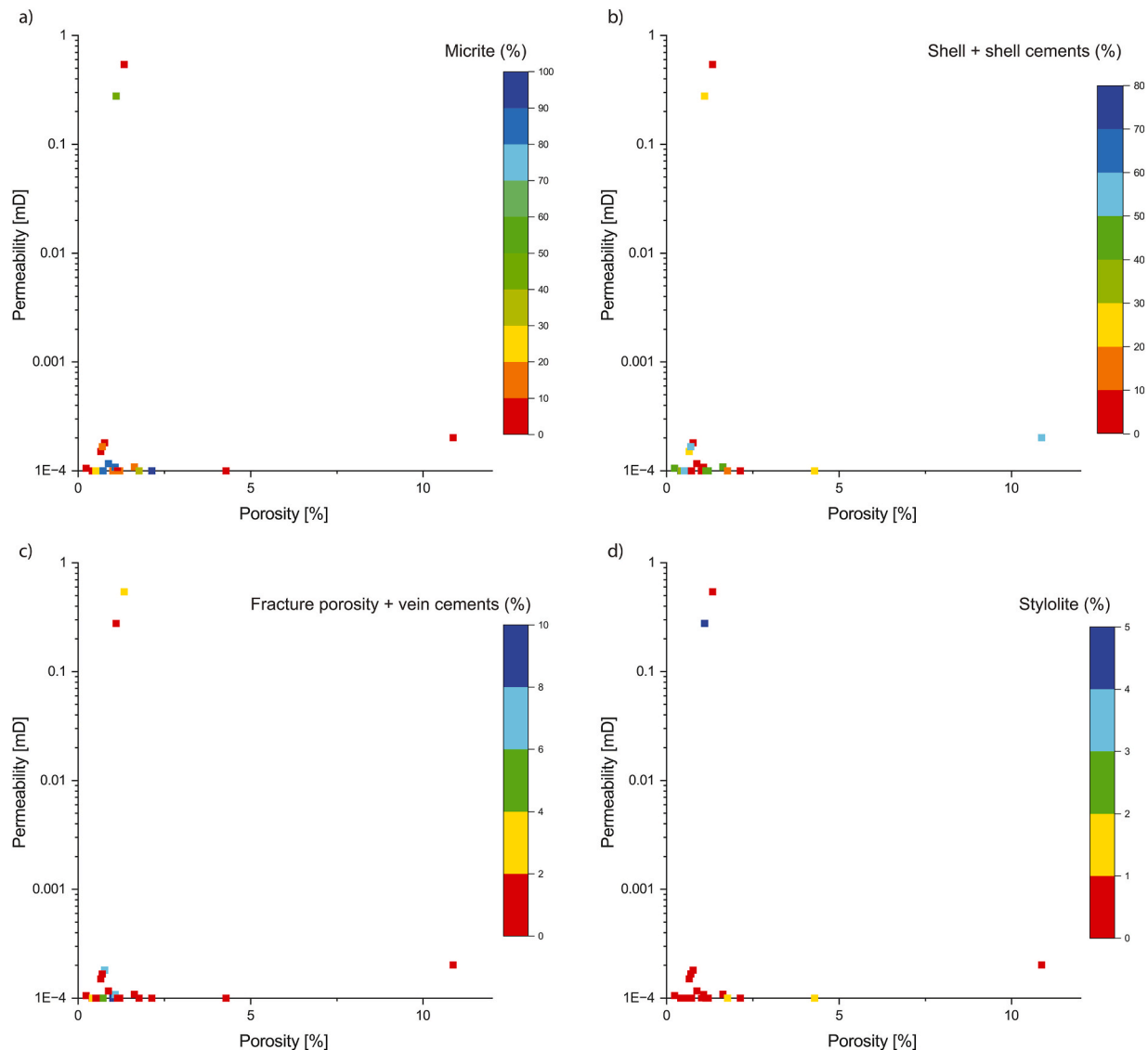
Fig. 12. Color-coded porosity-permeability plots linked with petrographic analyses. a) Micrite content, b) shells and recrystallized shells and their cements, c) fracture porosity + vein cements, permeability is higher in one sample containing fracture porosity + vein cements, d) stylolite, permeability is higher one the sample containing stylolites. Point counting data given in volume percent. Only individual samples show elevated permeability with occurring fracture porosity + vein cements and stylolites.

great circles and poles), the decameter-scale conjugate reverse kink-band with a breached kink-band boundary in the SSE show a dip direction/dip of 024/65 and 018/55 in the SSE part and of 157/59 and 160/66 in the NNW part (Figs. 14 and 15).

The calcite cementation on the breached kink band boundary show slickensides, which indicate reverse, strike-slip, and normal faulting, but clear cross-cutting relationships are absent. The conjugate kink band itself indicates compression with the maximum principal stress σ_1 in N-S direction (179/01), the intermediate principal stresses σ_2 is located in the intersection of the kink planes (088/33), minimum principal stress σ_3 (271/56) is normal to σ_2. In addition, normal faulting is observed at the topmost part of the quarry wall, at the transition to the Lower Keuper (Fig. 14, red arrow at topmost part).

To analyze if fracture intensities are affected by the presence of faults of the breached kink band, fracture intensity and clustering analyses are performed on a scanline parallel to the wall strike (348°). Clustering would imply that more fractures are encountered than can be expected in a random fracture arrangement, whereas anti-clusters would imply that fewer fractures are encountered than can be expected in a random

fracture arrangement.

For the scanline parallel to the NNW striking quarry wall with a fault zone of 2 m width (Fig. 14c), statistically significantly higher fracture intensities are observed in fracture sets (cf. Fig. 13) of all strike orientations (Kink 10°, 50°, 70°, 110° and 140° in Fig. 16), where major and minor peaks occur in different fracture sets (Figs. 16 and 17). However, for sets with strike orientations of 10°, 50°, 110°, and 140°, the higher fracture intensity is found in the hanging wall of the fault zone, while higher fracture intensities in the fracture set striking to 70° are found in the footwall of the breached kink band (to the right of the breached kink band in Fig. 16). Assessing the normalized correlation count, all fracture sets show significantly higher and lower peaks than a random fracture arrangement, except for set 70°, where only subordinary higher peaks than in a random arrangement can be determined. Sets 10° and 50° are mostly indistinguishable from random with only small peaks indicating clusters at 10s of cm length scales above the 95 % confidence limit. Sets 10° and 50°, however, show anti-clustering, indicating length scales, where fewer fractures than in a random arrangement are observed at length scales of three to 8 m. Set 70° is mostly indistinguishable from
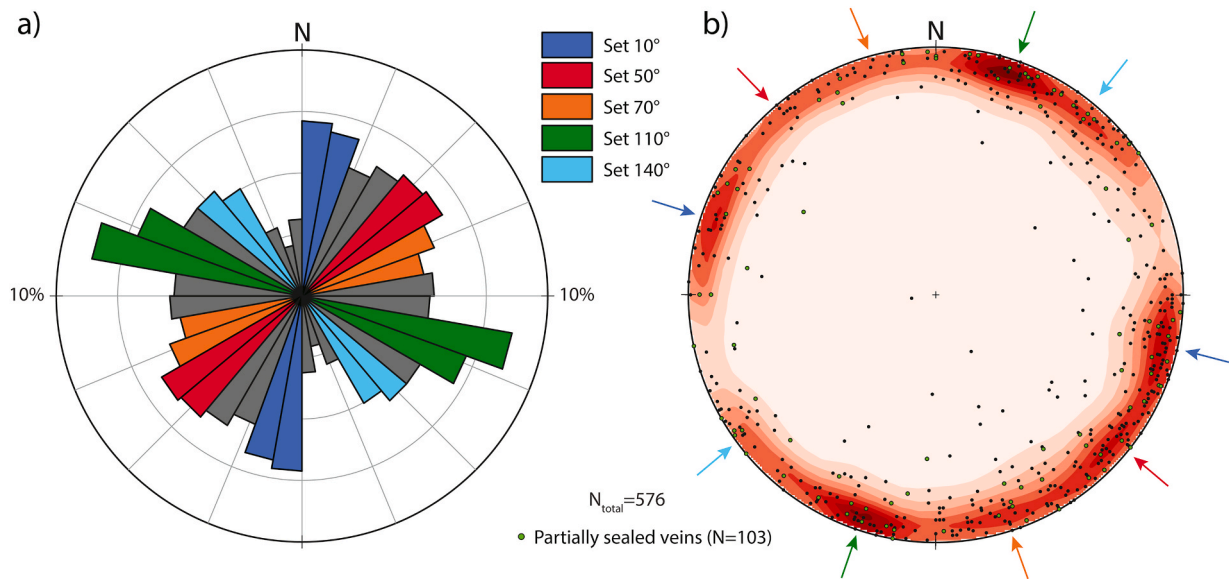
Fig. 13. Rose and pole point contour plot. a) Fracture strike of compass measurements for the Upper Muschelkalk and Lower Keuper from lithological columns and two scan lines (N = 576). Fracture sets were selected to represent the most prominent strike orientations (set 1 (10°), set 2 (50°), set 4 (110°)), strike orientations that are most suitably oriented in the present day stress field (set 1 (10°), set 4 (110°), set 5 (140°)), or to showcase that clustering analyses still require assessment of the stress field (set 3 (70°)). b) Fracture data plotted as poles to planes (lower hemisphere), arrows highlight highest pole densities, colors are related to facture sets in a). Partially sealed veins are highlighted as green poles (N = 103).

random. Set 110° aligns subparallel to the main faults of the breached kink band (kink band planes strike 114° and 108°). It shows regularly-spaced fractal clusters up to 1 m length scales and three to 5 m length scales, but also anti-clustering at length scales of one to 2 m and between five and 20 m. Fractal clusters themselves contain clusters which are consisting of smaller, self-similar, clusters (Marrett et al., 2018). Set 140° is mostly indistinguishable from random with only weak clusters at the meter scale and anti-clusters at length scales of four to 6 m.

Fracture intensities in the quarry wall perpendicular to the previous one, striking E to ENE (084°), for the same fracture set orientations striking 10°–140° (Base 10°, 50°, 70°, 110° and 140° in Fig. 17), show statistically significant clusters of higher fracture intensity in four of five strike sets, although no fault is present in the direct vicinity. Set 10° shows two minor and one larger peak, set 50° three larger peaks, set 70° show no statistically relevant intensity clusters, set 110° one interval with high fracture intensities and nine subsidiary peaks and set 140° show four larger peaks. Due to the shorter length of the scanlines, and fewer recorded fractures, the normalized correlation counts cannot be accurately assessed for all length scales. The normalized correlation count for set 10° is indistinguishable from random with only weak peaks above the confidence limit at 10s of centimeter and six to 7 m length scales. Set 50° show contains too few fracture data to accurately assess the correlation count. Set 70° is indistinguishable from random with no indication for clusters at any recorded length scales. Set 110° is indistinguishable from random with minor weak clusters at 0.5 m to 1 m length scales. Set 140° is mostly indistinguishable from random with weak clustering at 10 cm length scales and weak anti-clustering at seven to 8 m length scales.

4.5.1. Dilation and slip tendency

While the presence of fracture clusters in the vicinity of faults and the undisturbed lithology is promising to possibly enhance the fluid flow, the assessment of fracture orientation in relation to the present-day stress field is required to assess their influence on subsurface fluid flow. Therefore, we also assess dilation (T_d) and slip (T_s) tendencies.

T_d and T_s analyses are performed for all measured fractures (Fig. 18a and b) and separately for the fracture strike sets included in the clustering analyses (Fig. 18c and d). For the present-day stress field, values

from Meixner et al. (2014) derived for the nearby Bruchsal geothermal well (15 km NE of the studied quarry) were used. Low to medium T_d are observed for strike set 10°, medium T_d for strike set 110° and high T_d for strike set 140°. For slip tendencies, low to medium T_s for strike set 50°, 70°, 140° and high for strike set 110° and 10°.

5. Discussion

5.1. Lithology and depositional environment

The studied lithologies are composed of limestones and (marly) claystones from the Upper Muschelkalk (Meißner Fm.) from the base, to the Lower Keuper (Erfurt Fm.) at the top. The elevated marly claystone content and limited dolomite content aligns with the description of the basin facies (Hagdorn and Simon, 2021) (Fig. 1d), located toward the depositional center of the southern Germanic Basin. The topward decrease in marly claystone intercalations and relative increase in wacke- and packstones toward the top of the studied Upper Muschelkalk section and accompanying generally decreasing sGR response (Fig. 6) is in agreement with gamma-log measurements and lithology descriptions from boreholes in the studied area (Brunner and Simon, 1985). The data suggest a general shallowing upward trend, which is also described by e. g., Aigner (1985) and Aigner and Bachmann (1992) for the Germanic Basin and by Vollrath (1938) in the studied area. The uppermost part of the studied lithologies show some quartz pseudomorphs after sulphates, which may indicate a short period of brackish environment which lead to formation of evaporitic minerals, as e.g., described for authigenic euhedral quartz replacements after sulphates described by Friedman and Shukla (1980) for middle Silurian rocks.

Mud- and wackestones are interpreted to be deposited in low energy regimes, likely indicating an off-shoal environment recording occasional input from storm events in wackestones (Kostic and Aigner, 2004). The observed transition from micritic to shell-bearing layers is either sharp or undulating/bioturbated (Fig. 4), as also described by Mehl (1982) for tempestites in the southern Germanic Basin. In the upper part of the studied Upper Muschelkalk succession, rarely packstones are exposed, mostly composed of shell debris occasionally containing micritic envelopes, rarely composed of ooids, suggesting a more storm wave
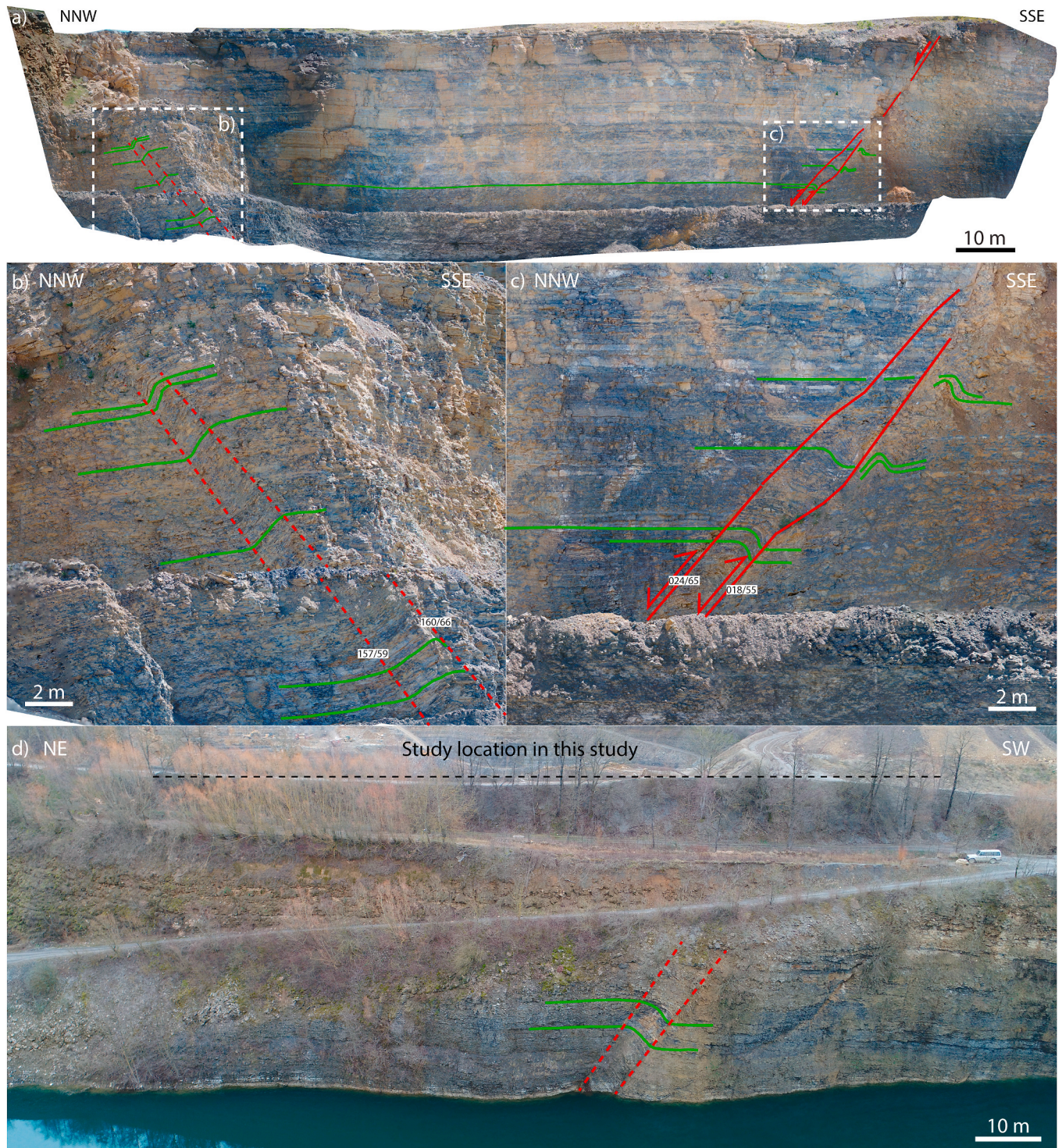
Fig. 14. Wall panel in the quarry with kink band recorded with drone. a) Overview of the wall striking NNW-SSE with kink band in the NNW part. b) Breached kink band in SSE part of the quarry. c) On top of the Upper Muschelkalk in a layer (a, red arrow) a normal fault is observed. d) Overview of a kink band occurring in the northern part of the quarry (Fig. 3a).

dominated environment, found in off-shoal areas and tempestites by Kostic and Aigner (2004).

The transition from the Upper Muschelkalk to Lower Keuper in the quarry is marked by a color change of the lithologies to beige claystones following the last grey claystone of the Vitriolschiefer (Fig. 5), and by an increase in the sGR signal (Fig. 6). This is in line with borehole gamma ray logs in the northern part of the southern Germanic Basin (Brunner and Simon, 1985; Etzold and Franz, 2005). In addition, the

interpretation of the lithostratigraphic boundary is supported by the observed phosphatic bonebed layer (Grenzbonebed, approx. 2–3 cm thick), and the thick-bedded blueish-grey limestones ("Blaubank", Figs. 5 and 6). The base of the bone bed overlays the upper boundary of the Muschelkalk unconformity in southwest Germany (Hagdorn and Simon, 2021).

As reconstructed for other Muschelkalk samples, a clear clustering of petrophysical values with lithotypes cannot be established (Kostic and
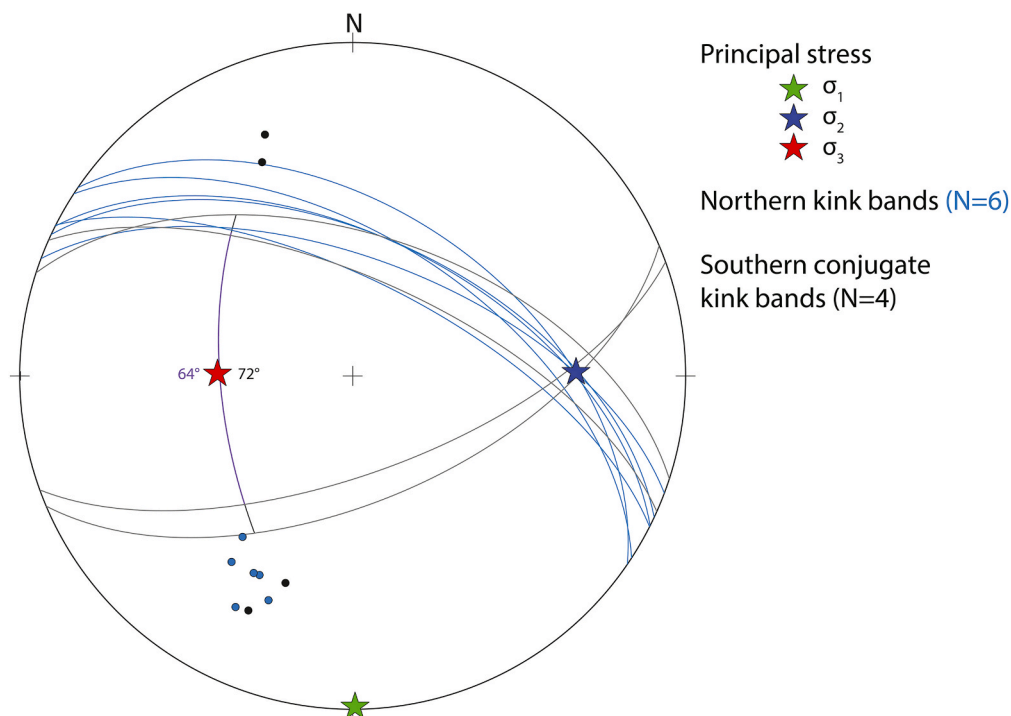
Fig. 15. Stereonet projection of kink bands in the northern quarry part (cf. Fig. 3a) in blue, and conjugate kink band planes as great circle and poles in black using OpenStereo. The opening angle for the conjugate kink band is 64°–72°, and the maximum principal stress σ_1 (green) is oriented N-S.

Aigner, 2004).

5.2. Paragenetic sequence

As no absolute ages are known, the paragenetic sequence is subdivided in early and burial diagenesis and based on cement parageneses and cross-cutting relationships.

Peloids or pellets, combined as peloids in this study as this term describes ovoid particles of micro- or cryptocrystalline appearance (McKee and Gutschick, 1969), are overall composed of calcitic micrite. In general, the origin of these allochems could be faecel pellets, algae, reworking of mud grains, recrystallization of bioclasts, or they can be formed in situ (Chafetz, 1986; Folk, 1959; Kazmierczak et al., 1996; Macintyre, 1985). Most of the crinoid fragments show a dusty appearance, which is due to micrite-filled intraparticle pores.

5.2.1. Early diagenesis of carbonate sediments

As some bioclasts (shells and crinoids) and peloids show either micritic envelopes or are completely composed of micrite the earliest interpreted alteration is the recrystallization/micritization of peloids and bioclasts. Micritization of ooids and the loss of former structures are also described by Brüderlin (1970) for Upper Muschelkalk biosparites in the southwestern part of the southern Germanic Basin and possibly due to algae, cyanobacteria, or boring (Bathurst, 1966). Especially boring and precipitation is often used to define the term micritic envelope, forming a cryptocrystalline isopachous rim on clasts which preserves these from alteration (Bathurst, 1966). Micritic envelopes are common in biosparites (Alexandersson, 1972 and references therein). Furthermore, micritic envelopes may indicate a former composition of high Mg-calcite or aragonite, as micritic envelopes form on skeletal particles composed of high Mg-calcite or aragonite in modern environments (Buchbinder and Friedman, 1970 and references therein).
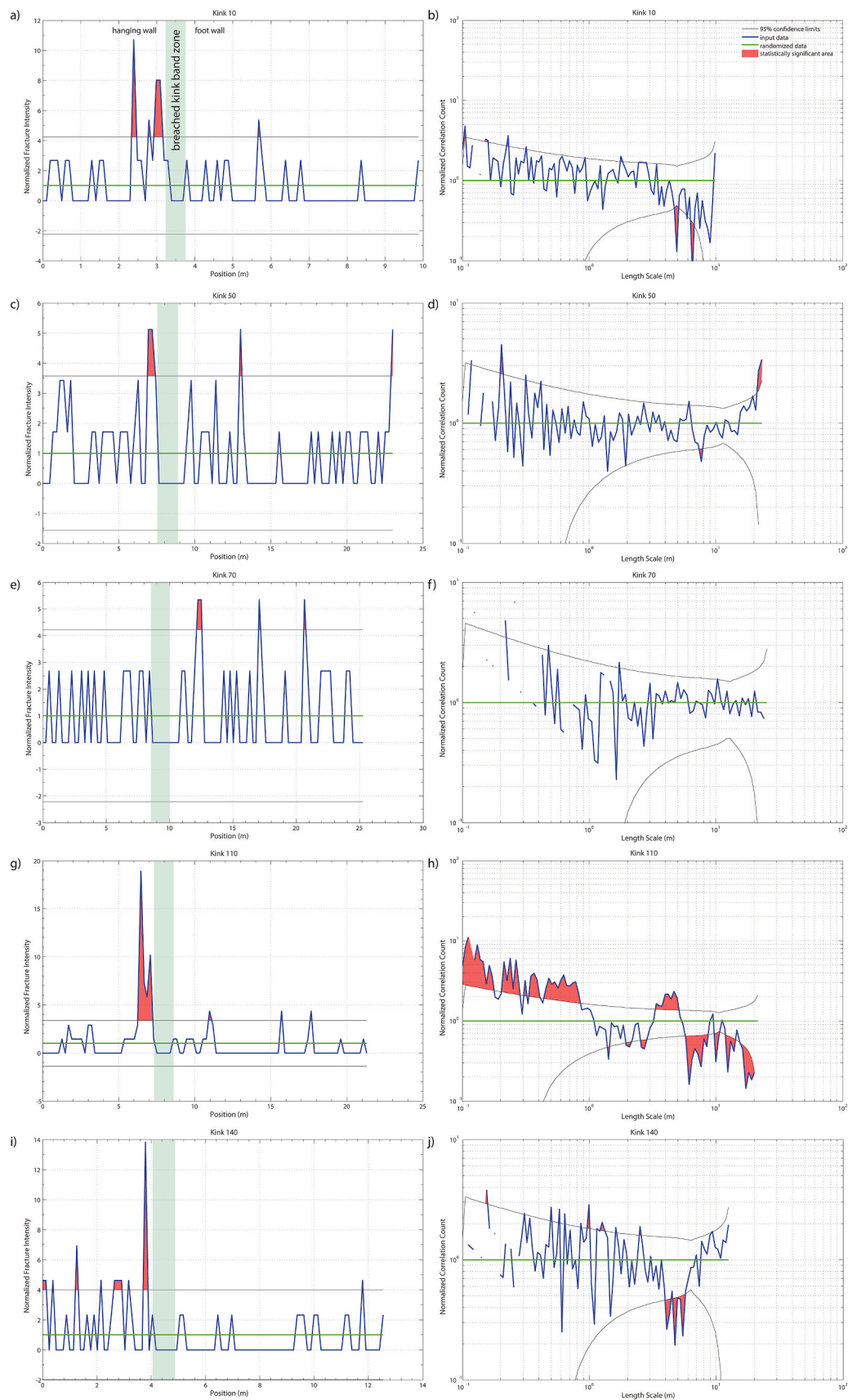
The previous presence of sulphates is indicated by bladed crystal mouldic morphologies which are now partially occluded by chert and clear macro quartz. The precipitation of sulphates is interpreted to occur during early diagenesis. Furthermore, former dissolution pores at the margin of sulphate molds are filled by calcite and Fe-calcite, indicating a formation of sulphates prior to carbonate cement precipitation.

Pyrite is found in e.g., shells or gastropods and encased in calcitic intraparticle cements. The formation of pyrite is interpreted to be early diagenetic likely due to bacterial sulphate reduction (BSR) (Berner, 1970), shortly after the deposition of bioclasts. This is a typical early diagenetic cement formation, also recorded in fine grained Jurassic limestones (Honjo et al., 1965).

Sparry replacive calcite cement grows from the rim of bioclasts into their center, which is encased by sparry ferroan calcite, where the crystal size also increases away from the test of the former shells. The occurrence of two generation of calcite spar is also described in e.g., Bathurst (1975), where the first generation is described to be caused by neomorphism in subaerial to submarine environments, leading to remaining preserved pore space, now also filled by Fe-calcite.

Based on the different optical properties of dolomite, two phases of dolomitization of former fossils or components as e.g., shells, ooids and peloids are observed in the samples (Fig. 7). The first phase (crystal size: 0.03–0.30 mm, avg.: 0.11 mm, dusty appearance mostly in center, non-pleochroitic) predominantly replaces ooids and peloids, whereas the intraparticle cements remain mostly unaltered by this phase. Active marine phreatic environments in shallow marine settings, especially in the mixing zone, are liable to form post-depositional dolomite by reflux down to 200 m below the surface or 300 m in marine dominated mixing zones (Budd, 1997; Cander, 1994; Gaswirth et al., 2007; Read et al., 2016). Furthermore, active marine phreatic environments are often characterized by high Mg-calcite precipitation, implying Mg availability in fluids (Longman, 1980). As ooids/peloids are partly or completely dolomitized, whereas the cements and matrix are unaltered, selective dolomitization is indicated. The dolomitization of individual ooids is in agreement with observations by Brüderlin (1970) for Upper Muschelkalk lithologies in the southern Germanic Basin. The onset of dolomitization of ooids and peloids is interpreted to pre-date the formation of cement phases filling interparticle porosity. The dolomitization of the matrix in individual samples (type II, crystal size 0.01–0.14 mm, avg.: 0.05 mm) (Fig. 7b) is interpreted to be related to temporarily

(caption on next page)

Fig. 16. CorrCount results for normalized fracture intensities (left column) and normalized correlation count (right column) for the wall striking 348° (NNW-SSE). Green areal marks the position of the breached kink band. Black lines indicate the boundaries of the 95 % confidence interval. Red highlighted areas (peaks) are exceeding the 95 % confidence interval and are therefore statistically significant. Green line is random value given by the NCC program, values in this area are not classified as clustered and thus indistinguishable. a) Statistically significant fractures of strike orientation 10° (red colored peaks) are limited to the footwall of the breached kink band, the values are (b) indistinguishable from random with only weak clusters above and beneath the lower confidence limit (N = 38). c) One peak is present at foot wall, and two on hanging wall, which are (d) are indistinguishable from random, as they do not clearly exceed the 95 % confidence interval (N = 59). e) Three peaks occur at hanging wall, which are (f) indistinguishable from random (N = 38). g) Main peak is present at foot wall and minor at hanging wall, which can be classified as (h) regularly-spaced fractal clusters with peaks and troughs over larger length scales (N = 69). i) Peaks occur at the foot wall, but are (j) indistinguishable from random with only weak clusters (N = 44).

hypersaline/evaporative or occasionally supratidal conditions, as also observed in samples from supratidal environment from the Jurassic (Rameil, 2008) or described by Zeeh and Geng (2001) in the Upper Muschelkalk in southwestern Germany.

Furthermore, saddle dolomite in shells, matrix replacive or as vein cement was observed as the third phase of dolomite. The dolomite types are distinguished by petrographic properties as pleochroism or extinction pattern, similar as in previous works (Zeeh and Geng, 2001). Similarly, the crystal sizes of our three dolomite types are in alignment with measured sizes by Zeeh and Geng (2001), where the crystal size of dolomites vary between <0.0 and 0.3 mm, classified as very fine crystalline dolomite type I, recrystallized dolomite type II and dolomite type III of subhedral to anhedral crystals with nonplanar texture.

The presence of isopachous/bladed fibrous calcite rim cement encasing partially replaced peloids/ooids (Fig. 7) and other skeletal fossil fragments, implies a formation during early diagenesis prior to mechanical compaction and following dolomitization. As the rim cements are interlocked in some samples, most interparticle porosity is occluded by this process. Generally, rim cements form in active marine phreatic environments (Longman, 1980) during early diagenesis (e.g., Geng and Zeeh, 1995). The rim cements showed an orange to dull orange luminescence (Fig. 8), whereas Geng and Zeeh (1995) described rim cements as dull orange or non-luminescent. The relative age constraint and low degree of compaction prior to cementation implies that all preceding alteration occurred in shallow water depth, potentially including short-lived supratidal conditions. Calcite and subordinary Fe-calcite cements encase isopachous fibrous/bladed calcite rim cement on particles and occlude either all or most of the remaining interparticle pore space following very minor mechanical compaction (Fig. 7e and f). They therefore have to post-date formation of rim cements and form during early diagenesis (cp. Immenhauser, 2022). As the calcite and Fe-calcite cements are partially replaced by chert and quartz laths, they have to pre-date their formation.

As some bioclasts are also replaced by chert and quartz laths replace intraparticle calcite cement, as well as fibrous/bladed rims cements and also partially replacing the rim cements on neighboring grains, the replacement by chert is interpreted to post-date calcite rim cement precipitation. Silicification is a prominent early diagenetic alteration in the mixing zone of active marine phreatic systems (Knauth, 1979) and the Muschelkalk (Geng, 1996). As chert and quartz are observed to fill bladed crystal molds, they are interpreted to have replaced sulphate minerals. Similar replacements are described in evaporitic settings in the US, forming at temperatures below 40 °C (Chowns and Elkins, 1974; Milliken, 1979). The early diagenetic dissolution of gypsum was also described by Geng (1996) for Muschelkalk deposits in the region. However, remaining intracrystalline pore space is visible in former sulphate molds lined by chert and quartz, indicating that the replacement was not pervasive and some sulphate may have been preserved, or that chert and quartz replacements stabilized the molds against compaction (Fig. 7). All chert and quartz replacements are interpreted to post-date the formation of initial cement phases and to be contemporaneous to the initial replacement of bioclasts by the same.

5.2.2. Burial diagenesis of carbonate sediments

The overall low preserved porosity (0–14.7 %, the latter in particles) indicates that most burial diagenetic alteration is restricted to

cementation of remaining pore spaces prior to further mechanical and chemical compaction, formation of fractures and (partial) cementation of these. Individual samples show stylolitization and formation of dissolution seams, which are an effect of increasing vertical effective stresses during burial.

The third phase of dolomite (type III) is the replacement of bioclasts and matrix which is characterized by larger crystal sizes (0.04–1.30, avg.: 0.27 mm), curved crystal outlines, undulose extinction, and are in some cases outlined by a phase of Fe-dolomite, and classified as saddle dolomite (Fig. 19). These features are also observed in shallow-water, mixed siliciclastic-carbonate sequences in Lower Triassic ramp succession in western Hungary (Győri et al., 2020). The undulose or sweeping extinction is caused by distorted crystal lattice structure (Warren, 2000). To form saddle dolomite, elevated temperatures of 60°–150 °C during burial are needed (Warren, 2000), indicating a burial depth of at least 2 km for a geothermal gradient of 30 °C/km.
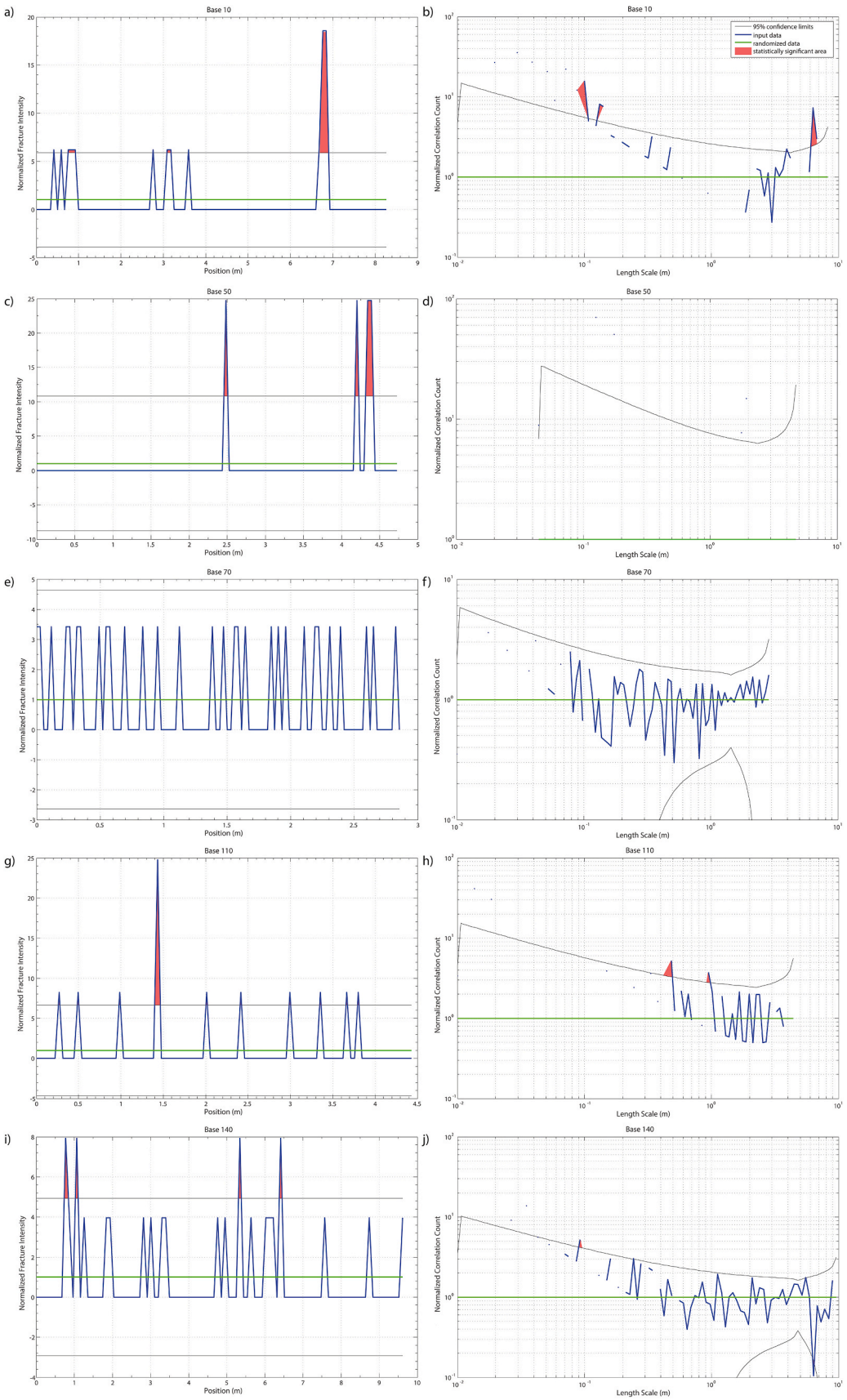
Saddle dolomite rhombs in shell fragments show a bright reddish luminescence and a non-luminescent rim using CL and a blue stain around some rims of saddle dolomite, indicating an increase of iron incorporated into dolomite, leading to non-luminescence (Pierson, 2006). Clay minerals de-water during mechanical compaction and provide Fe in solution (Miocic et al., 2020), as does pressure dissolution in Fe-bearing lithologies (Bathurst, 1975), which could be incorporated during further cementation of dolomite or calcite in the studied limestone-marly claystone section. The burial diagenetic dolomitization of shell fragments by saddle dolomite, was also interpreted by Geng and Zeeh (1995). As saddle dolomite and Fe-dolomite rims are encased in Fe-calcite, the saddle dolomite precipitation is pre-dating the last phase of Fe-calcite cementation in bioclasts. The matrix replacive, undulose dolomite (type III) pre-dates the formation of stylolites, as replacive dolomite is dissolved along them (Fig. 7j). In individual samples veins are displaced along stylolites, indicating that the formation of some veins predates the formation of stylolites (Toussaint et al., 2018).

5.2.3. Burial diagenesis of carbonate veins

As most veins in host rock samples and from a breached kink band crosscut all other diagenetic products, they are interpreted to post-date diagenetic alteration of the host rock. The paragenetic sequence (Fig. 19) of fracture filling carbonate cements is color coded with the observed colors from cathodoluminescence analyses (Figs. 8 and 6).

Pyrite at vein boundaries pre-dates or syn-dates the formation of the saddle dolomite vein (1, first vein generation). The occurrence of dolomite and pyrite in veins are also described in the Muschelkalk e.g., from the Mississippi-Valley-Type (MVT) Pb-Zn-Ag deposit near Wiesloch (see Fig. 1a) approximately 40 km north of our study area (Pfaff et al., 2010). The MVT deposits emplaced due to fluid mixing of ascending fluids in a releasing bend along the eastern Upper Rhine Graben fault in the Miocene (Pfaff et al., 2010). However, in this study pyrite most likely coprecipitates with saddle dolomite, as pyrite is not always present at the host rock – vein interface. The occurrence of saddle dolomite as fracture mineralization is also described by Geng and Zeeh (1995). Since saddle dolomite veins (generation 1) in a host rock sample also include (Fe-)calcite cements (generation 2), the formation of the latter is interpreted to postdate the formation of saddle dolomite (Fig. 19).

The earliest vein cement generation in a breached kink band sample includes (Fe-)calcite cements with similar luminescence characteristics

(caption on next page)

Fig. 17. CorrCount results for normalized fracture intensities and normalized correlation count for the undisturbed wall striking 084° (W–E). The 95 % confidence interval is given as black lines. Peaks are highlighted with red filling and exceeding the 95 % confidence interval and are thus statistically significant. The green line is what is classified as random value given by the NCC program, thus, values plotting this area are not classified as clustered and thus indistinguishable from random. a) One major and two minor peaks occur, which are (b) indistinguishable from random with only weak clusters above the confidence limit (N = 17). c) Three peaks occur, and the only (d) five points but are above the confidence limit, but cannot clearly be classified as cluster, because of the small amount of fracture values (N = 5). e) No statistically significant peaks occur; thus, the fractures are (f) indistinguishable from random (N = 30). g) One major and nine minor peaks are present, which are (h) indistinguishable from random with minor weak clusters above the confidence (N = 13). i) Four peaks are present which are (j) indistinguishable from random with weak clusters above and below the confidence limit (N = 26).
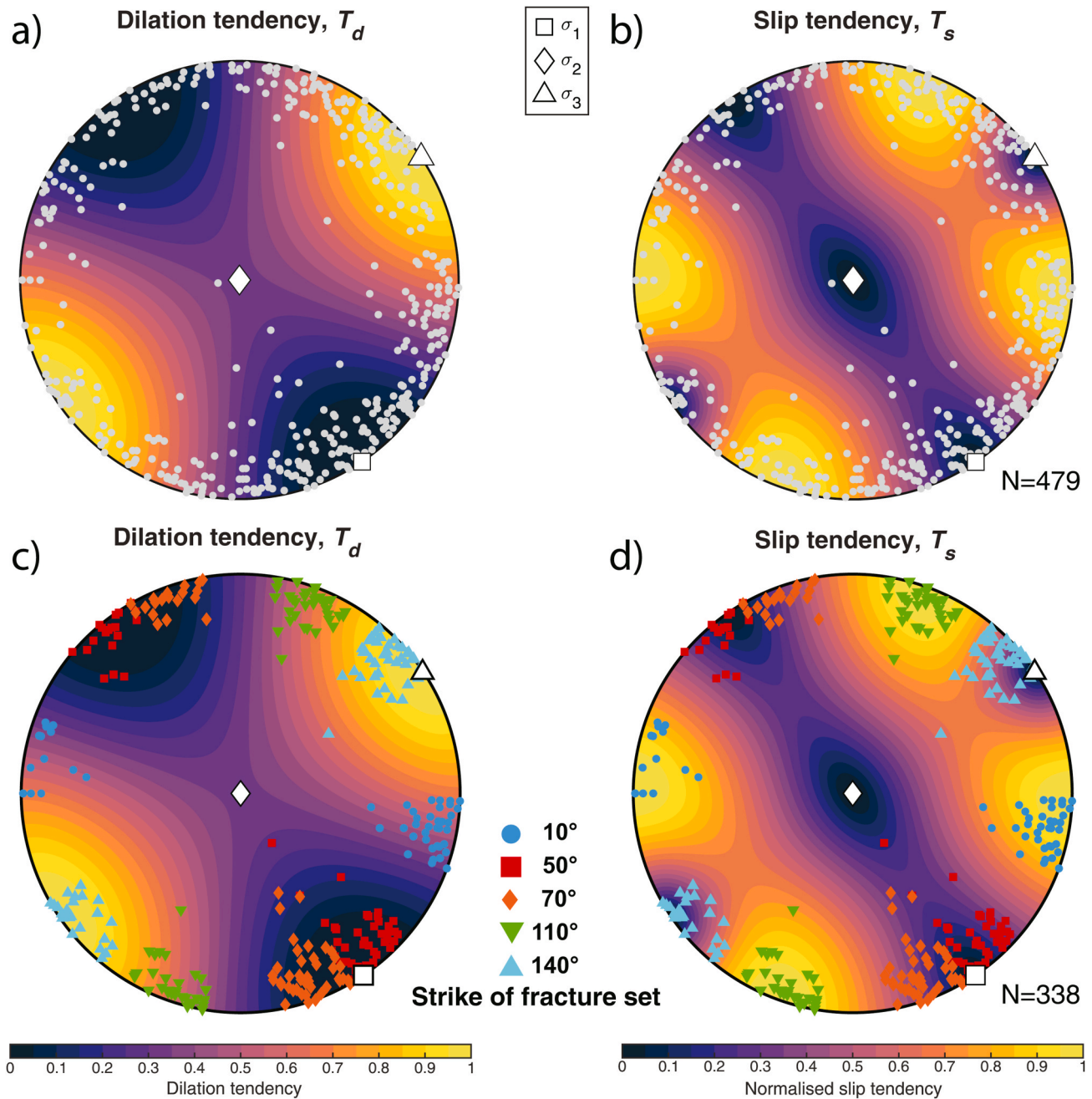

Fig. 18. Slip Dilation (T_d) and slip (T_s) tendency for clustered fracture strike sets (cf. Fig. 13). a), b) Dilation and slip tendency for all fractures of both scan lines. Fracture data for c) and d) are filtered in set classes as used for normalized correlation count. c) Dilation tendency for grouped striking sets in both scan lines, low to medium T_d for strike set 10°, medium T_d for strike set 110° and high for strike set 140°. d) Slip tendency for grouped striking sets in both scan lines, low to medium T_s for strike set 50°, 70°, 140° and high for strike set 110° and 10°.

as the vein cement generation 2 of the host rock samples. This composite vein and the generation 2 veins in the breached kink band samples are crosscut by a dull to non-luminescent (Fe-)calcite vein, which is interpreted to be vein generation 3. These are crosscut by a brighter (Fe-)calcite vein (generation 4) (Fig. 9). Veins from generation 5 are only found in a breached kink band sample (mostly dull Fe-calcite, Fig. 19)
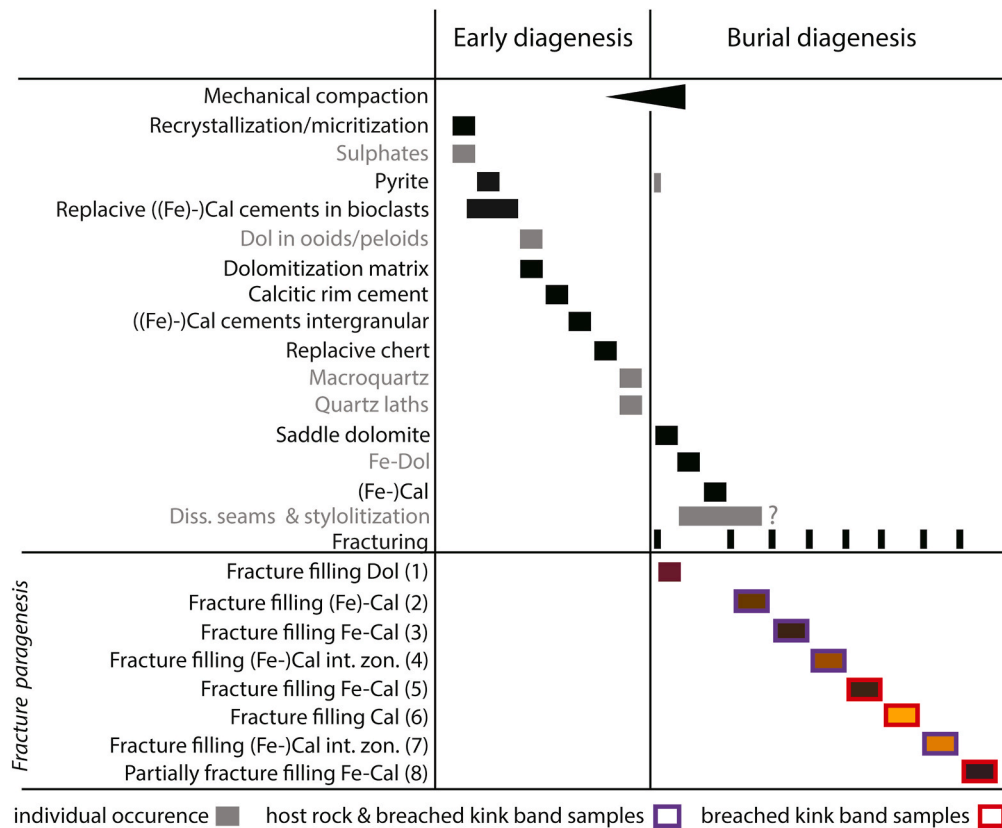
Fig. 19. Paragenetic sequence of the studied samples of Lower Keuper and Upper Muschelkalk. Black boxes highlight diagenetic products observed in all samples. Grey boxes correspond to diagenetic products only observed in individual samples. Colored boxes correspond to the observed CL color, no frame means observed only in host rock samples, purple frame means observed in host rock and breached kink band samples, and a red frame means observed only in breached kink band samples.

and are crosscut by very bright orange luminescing vein cement generation 6 and bright orange luminescing vein cement generation 7, which is found in both host rock and breached kink band samples. The partially fracture filling (Fe-)calcite generation 7 crosscuts generation 6 and always shows euhedral crystal facets in contact with fracture porosity. Vein generation 7 is furthermore encased by a dull to non-luminescent Fe-calcite vein cement (generation 8) in a breached kink band sample. Due to the observed paragenesis, generation 8 is likely the latest vein cement generation in the studied samples.

Overall, luminescence colors similar to vein cement generations 1–4 and 7 are found in host rock samples. Generations 2–8 (based on luminescence) are also found in the veins in the breached kink band boundary, highlighting a complex interplay of interacting vein sets.

5.3. Structures and fracture correlation to regional stress field

Previous studies on fractures and faults, as well as UAV aerial image assessments in the Knittlingen quarry (Merz et al., 2018, 2019) indicated that the Upper Muschelkalk was subject to normal faulting (Fig. 14, red arrow on the uppermost part). This was followed by later compression, resulting in decameter scale reverse kink bands with locally breached kink band boundaries with associated faults. Slickenlines on mineralized breached kink-band faults indicating normal, strike-slip, and reverse faulting.

5.3.1. Fracture orientation and history

The fracture sets were analyzed on two walls and additionally along the vertical lithological columns in the quarry (Fig. 13). The NNE-SSW striking fractures are parallel to the Upper Rhine Graben boundary, and are, in contrast to Meier et al. (2015), the fracture set with the

highest frequency. This may be related to the selection of scanline orientation. Therefore, our study compares two approximately orthogonal scanlines to capture all available fracture orientations. Because age data e.g., from calcite veins is missing, the corresponding fracture strike direction is related to published tectonic phases within Central Europe and the Upper Rhine Graben area (Dezayes and Lerouge, 2019; Kley and Voigt, 2008; Schumacher, 2002) (Fig. 2). However, this remains speculative as cross-cutting and abutting relationships are missing, and no large bedding planes exposing the fracture network were accessible.

The two most prominent fracture sets are NNE-SSW (parallel to the Upper Rhine Graben) and WNW-ESE, with additional sets striking NE-SW, ENE-WSW, NW-SE, W-E and NNW-SSE. Dezayes and Lerouge (2019) described three major sets: N-S, NE-SW/NW-SE and W-E in the sedimentary cover of the Upper Rhine Graben, Hemes (2008) described sets striking NNE-SSW, WNW-ESE, NW-SE, NNW-SSE, ENE-WSW and W-E for the Upper Muschelkalk lithologies on the eastern Graben shoulder approximately 40 km–50 km N to NE of the study location.

W-E striking fractures were related to pre-existing basement structures formed by the collapse of the Variscan range, which were reactivated during the Tertiary (Dezayes and Lerouge, 2019). Fracture sets striking NE-SW may be related to NE-SW directed Early Eocene Pyrenean collision and South Atlantic rifting during the Late Cretaceous until the Early Eocene (Kley and Voigt, 2008). During the Early/Middle Eocene, N-S striking fractures may have formed (Dezayes and Lerouge, 2019; Schumacher, 2002) (Fig. 2). NNE-SSW oriented compression during the Late Eocene most likely reactivated earlier faults and fractures (Meier et al., 2015; Schumacher, 2002).

The main rifting phase occurred during the Early Oligocene in an extensional setting (σ_3 oriented W-E to WNW-ESE) forming the normal faults of the Upper Rhine Graben (Schumacher, 2002). Simultaneously

the graben shoulders underwent pronounced rift flank uplift as well as erosion (Villemin et al., 1986).

Reactivation of the Upper Rhine Graben faults as dextral strike slip faults probably occurred during the Late Oligocene, where the central Upper Rhine Graben part formed a releasing bend (Schumacher, 2002) forming the Heidelberg pull apart basin (Fig. 1a) accumulating more than 3000 m of Tertiary and Quaternary deposits (Edel et al., 2007).

Hemes (2008) relate the occurrence of fractures striking ENE-WSW to Early Miocene changes in stress regime. The NW-SE oriented σ_1 stress direction was active during the Miocene and Pliocene, caused by the Alpine orogeny, also leading to a left lateral strike-slip phase of the graben-bounding faults (Dezayes and Lerouge, 2019; Schumacher, 2002; Ziegler, 1992).

5.3.2. Fracture clustering and T_d/T_s

Analyzing the fracture clustering using the normalized correlation count (NCC) method, random fracture arrangements could be distinguished from clustered and periodic arrangements. It is shown, that clustering does not only occur in fracture sets striking parallel to strike orientation of the breached kink band (fracture set 110°) (Fig. 14) or only in the vicinity of faults, but can also be present in a wall without a fault (Fig. 17). This extends previous datasets, which so far only linked higher fracture intensity to the vicinity of faults in the Muschelkalk in the same quarry (Meier et al., 2015).

Our results indicate the potential for elevated fracture intensities (fracture clusters) away from fault zones in the Muschelkalk. Exploration of fracture clusters may reduce the risk associated with drilling into fault zones and induced seismicity (e.g., Kruszewski et al., 2023).

Since the quarry is located on the eastern Upper Rhine Graben shoulder, which experienced approximately 800–1200 m uplift with respect to the same lithology in the graben center (Schwarz and Henk, 2005; Villemin et al., 1986), care has to be taken to match observed fracture orientations and intensities to the subsurface. However, for other limestone successions in northern Germany, this correlation could successfully be performed, where a variation of main strike direction is assumed to be caused by e.g., an influence of near-field stress perturbations around faults bounding the reservoir (e.g., Becker et al., 2018). Other studies report lower fracture intensities in outcrops than in the subsurface (Li et al., 2018).

The reported clusters show characteristics of regularly spaced fractal clusters or weak clustering with cluster spacings between 1 and 10 m and cluster widths <1 m and between 3 and 5 m (Figs. 16 and 17) (cf. Li et al., 2018; Marrett et al., 2018). If subsurface fracture orientations were similar, this analysis may guide horizontal drilling orientations and placements of perforated or open-hole sections in reservoir utilizations.

The normalized correlation count method performed on individual strike orientations with Terzaghi-corrected perpendicular fracture distances, deliver values for fracture intensities in the studied region, and are therefore less liable to artificially inflated fracture intensities if fractures of different strike sets are assessed in one combined dataset. This is essential, as only individual fracture sets are likely contributing to fluid flow in the studied region, based on the evaluation of dilation and slip tendencies. These have also been successfully used to assess the presence of individual hydrocarbon reservoirs in the Upper Rhine Graben, as varying fault strikes show different dilation and slip tendencies (Allgaier et al., 2023a). As mentioned by Li et al. (2018), the spatial arrangement of fracture clusters are important features referred to in industry application (Questiaux et al., 2010) and for reservoir models (Panza et al., 2016).

Dilation and slip tendencies of fracture surfaces as a function of present-day stress provide additional insights and quantify the individual reactivation potential of each cluster set (Barton et al., 1995; Becker et al., 2019a; Collettini and Trippetta, 2007; Ferrill et al., 1999, 2020; Morris et al., 1996). Slip potential for fracture strike set 110° and 10° are at highest, low to medium T_s is observed for strike set 50°, 70°, 140° using the present-day stress orientation and magnitude from Meixner

et al. (2014). The dilation tendency for fracture strike set 140° is high, and medium for sets 110° and 10° under present-day stress. The (strongly) clustered sets striking NNE-SSW (10°), WNW-ESE (110°), and NW-SE (140°) do therefore likely contribute to flow in the subsurface as they are suitably oriented, whereas the other orientations are unlikely to contribute to fluid flow, as they are unsuitably oriented in the present-day stress field. Fracture roughness classification was not part of this study. However, fractures which are shear displaced may show a misfit between surfaces and therefore shear dilation (Barton et al., 1985). Shear dilation of fractures can cause an enhancement of stress-resistant permanent permeability (e.g., Cheng and Milsch, 2021).

Additional controls on fluid flow in fractures and faults are chemical alterations and the formation of cements. Cements can act as bridges between fracture surfaces and thus preserve fracture porosity (Hilgers et al., 2004; Laubach et al., 2004). Our results indicate that samples containing partially cemented veins do preserve permeability higher than samples containing stylolites or the undisturbed host rock even at 30 MPa confining stress (Fig. 11). When the permeability measurements are normalized to the highest measured value of each sample as 1.0, the partially sealed vein retains 41 % of the initial permeability, the stylolite retains 16 %, and the undisturbed host rock retains only 11 % of the initial permeability if measurements at confining pressures of 1.25 (initial) and 30 MPa (highest) are compared. Partially sealed veins are interpreted to preserve permeability at depths (Gale et al., 2010; Lander and Laubach, 2015). Our laboratory results demonstrate for the first time the predicted permeability preservation due to partly open fractures as well as showing that stylolites can increase permeability. The lab measurements therefore confirm the applicability of literature models to reservoir scenarios, and imply the necessity for structural diagenetic assessment of samples from fractured reservoir plays.

Thus, the presence of partially sealed veins in all strike orientations (green dots in Fig. 13b) shows that in addition to suitably oriented fracture orientations in the present-day stress field, partial sealing can also preserve fluid pathways in all studied fracture orientations. This highlights that in addition to T_d and T_s evaluations, the study of structural diagenetic properties of partially sealed veins is necessary to fully understand the fluid flow system, because they additionally contribute to the fluid flow network in fractured carbonates irrespective of the current present-day stress.

5.3.3. Kink band formation

The reconstructed σ_1-orientation during kink band formation is N-S (Fig. 15), matching the Middle Eocene stress field orientation related to the Alpine orogeny (Fig. 2). Additionally, reactivation of the kink band could have occurred during the Miocene, where also the releasing bend in Wiesloch (~30 km N of the study location) is interpreted to be formed (Pfaff et al., 2010).

Calcite cemented fault planes are exposed along the breached kink band boundary (Fig. 9g and h). Microstructures show euhedral crystal facets in contact with fracture porosity, with some fracture porosity locally preserved in the breached kink band. The breached kink band boundaries indicate thrust, normal, and strike slip movement, the latter likely related to fault reactivation, e.g., synchronous with the Miocene MVT Pb-Zn impregnation near Wiesloch (Fig. 1a–Pfaff et al., 2010) and the subsidence of the pull-apart basins near Heidelberg and Rastatt (Fig. 1a and Böcker et al., 2017; Gabriel et al., 2013). Normal fault reactivation by younger reverse faults was also reported from the eastern graben fault (Ziegler, 1992).

5.4. Reservoir quality controls

The matrix reservoir quality of the Upper Muschelkalk and Lower Keuper limestones is influenced by small grain size (micrite to microspar), early and burial diagenetic cementation with mostly (Fe-)calcite and dolomite/saddle dolomite (Fig. 19). Both result in low porosity (0.13–10.9 %) and low permeability (<0.0001–9.7 mD) of the host rock.

Permeability is only enhanced where open or partially sealed fractures are present (9.7 mD) and porosity is enhanced where druses are present (10.9 %). Samples containing partially sealed veins, measured under higher confining pressures (up to 30 MPa) indicate that permeability is preserved, as the permeability measurement using 1.25 MPa confining stress do not represent the stresses in the subsurface at depths. This assessment is also supported by lower pressure sensitivity coefficient of permeability (γ) in the sample containing partially sealed vein, indicating a lower stress sensitivity than in samples containing a stylolite or of the undisturbed host rock. While permeability in a reservoir is not controlled by the permeability of an individual fracture, the fracture network (fracture lengths and connectivity) requires further analyses in the studied region. However, as partially sealed fractures are observed in all strike orientations (green points in Fig. 13b), it is likely that they will contribute to reservoir-scale fluid migration.

Rock typing shows that only one sample showed positive correlation with micrite and permeability (Fig. 12a), but this is solely due to higher amount of fracture porosity and vein cements (Fig. 12d). Micrite therefore has no positive effect on porosity or permeability in this study. However, the micrite content can enhance porosity due to microporosity in other limestones (Ölmez et al., 2024). Also, the content of shells (with primary features) and recrystallized shells does not correlate to enhanced porosity or permeability (Fig. 12b), whereas the stylolites (Fig. 12c), fracture porosity, and partially sealed veins (Fig. 12d) appear to positively affect permeability in individual samples. However, stylolite-bearing samples show a more drastic decrease in permeability at higher confining pressures as samples containing partially sealed veins (Fig. 11).

Previous studies on Muschelkalk samples highlight, however, that matrix porosity and permeability may be locally enhanced in porous coquinite layers, and peloid or ooid grainstones formed in shoal areas (Koehrer et al., 2010; Petrovic and Aigner, 2017; Warnecke and Aigner, 2019). Other studies on less cemented samples from the Upper Muschelkalk in SW Germany show a weak positive correlation (Ruf and Aigner, 2004), which is not similar to this study, and highlights the heterogeneity found in the Muschelkalk in south-western Germany.

The Lower Keuper lithologies with higher amounts of claystones and some smaller interbeds of limestones are more prone to act as a seal on top of the fractured Upper Muschelkalk reservoir. This is similar to Upper Muschelkalk reservoirs in NE Netherlands (Pöppelreiter et al., 2004). Fractured carbonates in Muschelkalk thus may contribute to accessible reservoir volumes in the Upper Rhine Graben.

6. Conclusion

Pervasively sealed veins, fine grained mudstones or pervasive early diagenetic pore space cementation have been shown to generally reduce matrix reservoir quality in the presented study. Thus, the reservoir quality in the tight carbonate reservoir is solely related to natural fractures and partially sealed veins, and to some extent stylolites if they are aligned parallel to fluid flow direction.

The measurement of plugs containing partially sealed veins under elevated confining pressure of 30 MPa show permeabilities of 0.13 mD, upon normalizing the permeability measurements to the maximum recorded value of each sample, this sample retains c. 41 % of the initial permeability as opposed to only 11 % of retained permeability in an undisturbed host rock sample.

Decameter-scale reverse kink-bands form reverse faults along breached kink band boundaries and indicate a N-S compressional tectonic phase during formation. They thus formed by Alpine far-field stress during the Eocene in the studied region, which were not documented so far. Kink-related reverse and thrust faults were locally reactivated by strike slip and may be synchronous with Miocene shear along the NNE striking Rhine graben fault, associated with pull apart basins and MVT-mineralization in the region.

Fracture clusters striking 10°, 110° and 140° occur in the undisturbed host rock, indicating, that fracture clusters are not necessarily restricted to faults or their damage zone. Integrating shear and dilation tendency analyses with clustering analyses highlight that likely only fracture clusters striking NNE-SSW, WNW-ESE, and NW-SE are potential fluid conduits and thus of importance for geoenergy application, if these fracture sets are also developed in the subsurface.

Appendix A. Supplementary data

Supplementary data to this article can be found online at https://doi.org/10.1016/j.jsg.2025.105566.

Data availability

Research data is provided as an electronic supplementary data file.

References

Agosta, F., Alessandroni, M., Antonellini, M., Tondi, E., Giorgioni, M., 2010. From fractures to flow: a field-based quantitative analysis of an outcropping carbonate reservoir. Tectonophysics 490, 197–213.

Ahorner, L., 1975. Present-day stress field and seismotectonic block movements along major fault zones in central Europe. Tectonophysics 29, 233–249.

Ahr, M., 2008. Geology of Carbonate Reservoirs: The Identification, Description, and Characterization of Hydrocarbon Reservoirs in Carbonate Rocks.

Aigner, T., 1985. Storm Depositional Systems - Dynamic Stratigraphy in Modern and Ancient shallow-marine Sequences, 1 ed. Springer, Berlin, Heidelberg.

Aigner, T., 1986. Dynamische Stratigraphie des Hauptmuschelkalks im südwestdeutschen Becken. Jahreshefte der Gesellschaft für Naturkunde in Württemberg Bd 141, 33–55, 1986.

Aigner, T., Bachmann, G.,H., 1992. Sequence-stratigraphic framework of the German Triassic. Sediment. Geol. 80, 115–135.

Alexandersson, T., 1972. Micritization of carbonate particles: processus of precipitation and dissolution in modern shallow-marine sediments. Bull. Geol. Inst. Univ. Upps 201–236.

Allgaier, F., Busch, B., Hilgers, C., 2023a. Fault leakage and reservoir charging in the upper rhine graben, Germany – assessment of the leopoldshafen fault bend. Mar. Petrol. Geol. 156, 106428.

Allgaier, F., Busch, B., Niederhuber, T., Quandt, D., Müller, B., Hilgers, C., 2023b. Fracture network characterisation of the naturally fractured upper Carboniferous

sandstones combining outcrop and wellbore data, Ruhr Basin, Germany. Z. Dtsch. Ges. Geowiss. 173, 599–623.

Almansour, A., Laubach, S.E., Bickel, J.E., Schultz, R.A., 2020. Value-of-Information analysis of a fracture prediction method. SPE Reservoir Eval. Eng. 23, 811–823.

Amann-Hildenbrand, A., Dietrichs, J.P., Krooss, B.M., 2016. Effective gas permeability of tight gas sandstones as a function of capillary pressure – a non-steady-state approach. Geofluids 16, 367–383.

Anders, B., Beccaletto, L., Capar, L., Mermy, D.C., Dezayes, C., Dresmann, H., Elsass, P., Fehn, C., Fischer, G., Franz, M., Haneke, J., Huggenberger, P., Kärcher, T., Krzyzanowski, J., Nitsch, E., Oliviero, G., Prestel, R., Rodat, C., Rupf, I., Schuff, J., Siemon, S., Sokol, G., Storz, R., Tesch, J., Urban, S., Weidenfeller, M., Wielandt-Schuster, U., Wirsing, G., Zumsprekel, H., 2013. Geopotenziale des tieferen Untergrundes im Oberrheingraben: Fachlich-Technischer Abschlussbericht des INTERREG-Projekts GeORG, Teil 4: atlas. LGRB-Informationen, Freiburg i. Br./Mainz/Strasbourg/Basel.

Bahrami, H., Rezaee, R., Hossain, M., 2012. Characterizing natural fractures productivity in tight gas reservoirs. J. Pet. Explor. Prod. Technol. 2, 107–115.

Barton, C.A., Zoback, M.D., Moos, D., 1995. Fluid flow along potentially active faults in crystalline rock. Geology 23, 683–686.

Barton, N., Bandis, S., Bakhtar, K., 1985. Strength, deformation and conductivity coupling of rock joints. Int. J. Rock Mech. Min. Sci. Geomech. Abstracts 22, 121–140.

Bathurst, R.G.C., 1966. Boring algae, micrite envelopes and lithification of molluscan biosparites. Geol. J. 5, 15–32.

Bathurst, R.G.C., 1975. Carbonate sediments and their diagenesis. Dev. Sedimentol. 658.

Becker, I., Birgit, M., Koehrer, B., Jelinek, W., Hilgers, C., 2019a. Present-day stress control on fluid migration pathways: case study of the zechstein fractured carbonates, NW-Germany. Mar. Petrol. Geol. 103, 320–330.

Becker, I., Koehrer, B., Hilgers, C., 2019b. Correlating three Upper Permian Zechstein-2-Carbonate outcrops across the eichsfeld-altmark swell - facies, reservoir properties, and outcrop analogue potential. Z. Dtsch. Ges. Geowiss. 169, 517–531.

Becker, I., Koehrer, B., Jelinek, W., Bahlvogel, M., Hilgers, C., 2018. Comparing fracture statistics from outcrop and reservoir data using conventional manual and t-LiDAR derived scanlines in Ca2 carbonates from the southern Permian Basin, Germany. Mar. Petrol. Geol. 95, 228–245.

Becker, I., Wüstefeld, P., Koehrer, B., Felder, M., Hilgers, C., 2017. Porosity and permeability variations in a tight gas sandstone reservoir analog, Westphalian D, Lower Saxony basin, NW Germany: influence of depositional setting and diagenesis. J. Petrol. Geol. 40, 363–389.

Berner, R.A., 1970. Sedimentary pyrite formation. Am. J. Sci. 268, 1–23.

Bing maps, 2025. https://www.bing.com/maps?cp=49.028437%7E8.735134&lvl=17.4&style=h. (Accessed 13 May 2025).

Böcker, J., Littke, R., Forster, A., 2017. An overview on source rocks and the petroleum system of the central upper rhine graben. Int. J. Earth Sci. 106, 707–742.

Böcker, J.J., 2015. Petroleum System and Thermal History of the Upper Rhine Graben - Implications from Organic Geochemical Analyses, oil-source Rock Correlations and Numerical Modelling. Fakultät für Georessourcen und Materialtechnik. Rheinisch-Westfälische Technische Hochschule Aachen, Aachen, p. 168.

Bonnet, E., Bour, O., Odling, N.E., Davy, P., Main, I., Cowie, P., Berkowitz, B., 2001. Scaling of fracture systems in geological media. Rev. Geophys. 39, 347–383.

Bossennec, C., Géraud, Y., Böcker, J., Klug, B., Mattioni, L., Sizun, J.-P., Sudo, M., Moretti, I., 2021. Evolution of diagenetic conditions and burial history in buntsandstein Gp. fractured sandstones (Upper Rhine Graben) from in-situ δ18O of quartz and 40Ar/39Ar geochronology of K-feldspar overgrowths. Int. J. Earth Sci. 110, 2779–2802.

Brüderlin, M., 1970. Beiträge zur Lithostratigraphie und Sedimentpetrographie des Oberen Muschelkalks im südwestlichen Baden-Württemberg. Teil II: Sedimentpetrographie. Jahresberichte und. Mitteilungen des Oberrheinischen Geologischen Vereins 52, 175–209.

Brunner, H., Simon, T., 1985. Lithologische Gliederung von Profilen aus dem Oberen Muschelkalk im nördlichen Baden-Württemberg anhand der natürlichen Gamma-Strahlungsintensität der Gesteine. Jahresber. Mittl. Oberrheinischen Geol. Vereins 67, 289–299.

Buchbinder, B., Friedman, G.M., 1970. Selective dolomitization of micritic envelopes; a possible clue to original mineralogy. J. Sediment. Res. 40, 514–517.

Budd, D.A., 1997. Cenozoic dolomites of carbonate islands: their attributes and origin. Earth Sci. Rev. 42, 1–47.

Burchette, T., Britton, S., 1985. Carbonate Facies Analysis in the Exploration for Hydrocarbons: a case-study from the Cretaceous of the Middle East, 18. Geological Society, London, Special Publications, pp. 311–338.

Burchette, T.P., 2012. Carbonate Rocks and Petroleum Reservoirs: a Geological Perspective from the Industry, 370. Geological Society, London, Special Publications, pp. 17–37.

Busch, B., Adelmann, D., Herrmann, R., Hilgers, C., 2022a. Controls on compactional behavior and reservoir quality in a Triassic buntsandstein reservoir, Upper Rhine Graben, SW Germany. Mar. Petrol. Geol. 136, 105437.

Busch, B., Becker, I., Koehrer, B., Adelmann, D., Hilgers, C., 2019. Porosity evolution of two upper Carboniferous tight-gas-fluvial sandstone reservoirs: impact of fractures and total cement volumes on reservoir quality. Mar. Petrol. Geol. 100, 376–390.

Busch, B., Böcker, J., Hilgers, C., 2024. Improved reservoir quality assessment by evaluating illite grain coatings, quartz cementation, and compaction – case study from the Buntsandstein, Upper Rhine Graben, Germany. Geoenergy Sci. Eng. 241, 213141.

Busch, B., Spitzner, A.-D., Adelmann, D., Hilgers, C., 2022b. The significance of outcrop analog data for reservoir quality assessment: a comparative case study of Lower Triassic buntsandstein sandstones in the Upper Rhine Graben. Mar. Petrol. Geol. 141, 105701.

Cander, H.S., 1994. An example of mixing-zone dolomite, middle Eocene avon park formation, floridan aquifer system. J. Sediment. Res. 64, 615–629.

Carlos de Dios, J., Delgado, M.,A., Martínez, C., Ramos, A., Álvarez, I., Marín, J.,A., Salvador, I., 2017. Hydraulic characterization of fractured carbonates for CO2 geological storage: experiences and lessons learned in hontomín technology development plant. Int. J. Greenh. Gas Control 58, 185–200.

Cawood, A.,J., Bond, C.,E., Howell, J.,A., Butler, R.,W.H., Totake, Y., 2017. LiDAR, UAV or compass-clinometer? Accuracy, coverage and the effects on structural models. J. Struct. Geol. 98, 67–82.

Chafetz, H.S., 1986. Marine peloids: a product of bacterially induced precipitation of calcite. J. Sediment. Res. 56, 812–817.

Cheng, C., Milsch, H., 2021. Hydromechanical investigations on the self-propping potential of fractures in tight sandstones. Rock Mech. Rock Eng. 54, 5407–5432.

Choquette, P.W., Pray, L.C., 1970. Geologic nomenclature and classification of porosity in sedimentary carbonates. AAPG (Am. Assoc. Pet. Geol.) Bull. 54, 207–250.

Chowns, T.M., Elkins, J.E., 1974. The origin of quartz geodes and cauliflower cherts through the silicification of anhydrite nodules. J. Sediment. Res. 44, 885–903.

Clauser, C., Villinger, H., 1990. Analysis of conductive and convective heat transfer in a sedimentary basin, demonstrated for the rheingraben. Geophys. J. Int. 100, 393–414.

Collettini, C., Trippetta, F., 2007. A slip tendency analysis to test mechanical and structural control on aftershock rupture planes. Earth Planet Sci. Lett. 255, 402–413.

David, C., Wong, T.-F., Zhu, W., Zhang, J., 1994. Laboratory measurement of compaction-induced permeability change in porous rocks: implications for the generation and maintenance of pore pressure excess in the crust. Pure Appl. Geophys. 143, 425–456.

Dewey, J.F., 1965. Nature and origin of kink-bands. Tectonophysics 1, 459–494.

Dezayes, C., Lerouge, C., 2019. Reconstructing paleofluid circulation at the Hercynian basement/mesozoic sedimentary cover interface in the Upper Rhine Graben. Geofluids, 4849860, 2019.

Dickson, J.A.D., 1965. A modified staining technique for carbonates in thin section. Nature 205, 587.

Dunham, R.J., 1962. Classification of carbonate rocks according to depositional texture. In: Ham, W.E. (Ed.), Classification of Carbonate Rocks - a Symposium. AAPG, pp. 108–121.

Durst, H., 1991. Aspects of exploration history and structural style in the rhine graben area. Generation, accumulation. and Production of Europe's Hydrocarbons, pp. 247–261.

Edel, J.B., Schulmann, K., Rotstein, Y., 2007. The Variscan tectonic inheritance of the Upper Rhine Graben: evidence of reactivations in the lias, late Eocene–Oligocene up to the recent. Int. J. Earth Sci. 96, 305–325.

Ehrenberg, S.N., Eberli, G.P., Keramati, M., Moallemi, S.A., 2006. Porosity-permeability relationships in interlayered limestone-dolostone reservoirs. AAPG (Am. Assoc. Pet. Geol.) Bull. 90, 91–114.

Elliott, S.J., Forstner, S.R., Wang, Q., Corrêa, R., Shakiba, M., Fulcher, S.A., Hebel, N.J., Lee, B.T., Tirmizi, S.T., Hooker, J.N., Fall, A., Olson, J.E., Laubach, S.E., 2025. Diagenesis is key to unlocking outcrop fracture data suitable for quantitative extrapolation to geothermal targets. Front. Earth Sci. 13, 1–38.

Etzold, A., Franz, M., 2005. Ein Referenzprofil des Keupers im Kraichgau - zusammengesetzt aus mehreren Kernbohrungen auf Blatt 6718 Wiesloch (Baden-Württemberg), LGRB-Informationen, 17, pp. 25–124.

Ferrill, D.A., Smart, K.J., Morris, A.P., 2020. Fault failure modes, deformation mechanisms, dilation tendency, slip tendency, and conduits v. seals. In: Ogilvie, S.R., Dee, S.J., Wilson, R.W., Bailey, W.R. (Eds.), Integrated Fault Seal Analysis. Geological Society of, London.

Ferrill, D.A., Winterle, J., Wittmeyer, G.W., Sims, D., Colton, S.L., Armstrong, A., 1999. Stressed Rock Strains Groundwater at Yucca Mountain, Nevada. GSA Today.

Finkbeiner, T., Barton, C.A., Zoback, M.D., 1997. Relationships among in-situ stress, fractures and faults, and fluid flow: Monterey Formation, Santa Maria Basin, California. AAPG (Am. Assoc. Pet. Geol.) Bull. 81, 1975–1999.

Folk, R.L., 1959. Practical petrographic classification of limestones 1. AAPG (Am. Assoc. Pet. Geol.) Bull. 43, 1–38.

Folk, R.L., 1974. The natural history of crystalline calcium carbonate; effect of magnesium content and salinity. J. Sediment. Res. 44, 40–53.

Franz, M., Kaiser, S.I., Fischer, J., Heunisch, C., Kustatscher, E., Luppold, F.W., Berner, U., Röhling, H.G., 2015. Eustatic and climatic control on the Upper Muschelkalk Sea (late Anisian/Ladinian) in the central European Basin. Global Planet. Change 135, 1–27.

Friedman, G.M., Shukla, V., 1980. Significance of authigenic quartz euhedra after sulfates; example from the lockport formation (Middle Silurian) of New York. J. Sediment. Res. 50, 1299–1304.

Gabriel, G., Ellwanger, D., Hoselmann, C., Weidenfeller, M., Wielandt-Schuster, U., 2013. The Heidelberg Basin, Upper Rhine Graben (Germany): a unique archive of Quaternary sediments in central Europe. Quat. Int. 292, 43–58.

Gale, J.,F.W., Lander, R.,H., Reed, R.,M., Laubach, S.,E., 2010. Modeling fracture porosity evolution in dolostone. J. Struct. Geol. 32, 1201–1211.

Garland, J., Neilson, J., Laubach, S.E., Whidden, K.J., 2012. Advances in Carbonate Exploration and Reservoir Analysis, 370. Geological Society, London, Special Publications, pp. 1–15.

Gaswirth, S.B., Budd, D.A., Lang Farmer, G., 2007. The role and impact of freshwater–seawater mixing zones in the maturation of regional dolomite bodies within the proto Floridan Aquifer, USA. Sedimentology 54, 1065–1092.

Geng, A., 1996. Diagenesis of the Middle Triassic Muschelkalk, Southwestern Germany. Heidelberg University, p. 86.

Geng, A., Zeeh, S., 1995. Diagenesis of Middle Triassic Muschelkalk carbonate rocks of the Rhine graben and adjacent areas (southwest Germany). Z. Dtsch. Geol. Ges. 146, 372–385.

Girardeau-Montaut, D., 2017. Cloudcompare (Version 2.10alpha).

Gomez-Rivas, E., Martín-Martín, J.D., Bons, P.,D., Koehn, D., Griera, A., Travé, A., Llorens, M.-G., Humphrey, E., Neilson, J., 2022. Stylolites and stylolite networks as primary controls on the geometry and distribution of carbonate diagenetic alterations. Mar. Petrol. Geol. 136, 105444.

Grohmann, C.H., Campanha, G.A.C., 2010. Openstereo: Open Source, cross-platform Software for Structural Geology Analysis.

Gutteridge, P., ten Veen, J., Dewit, J., Garland, J., Riva, A., Mozafari, M., Jaarsma, B., van Melle, T., 2025. Regional assessment of the ultra-deep geothermal (UDG) reservoir quality and potential of the Dinantian Zeeland formation, the Netherlands. Geological Society, London, Special Publications 548. SP548-2023-2106.

Győri, O., Haas, J., Hips, K., Lukoczki, G., Budai, T., Demény, A., Szőcs, E., 2020. Dolomitization of shallow-water, mixed siliciclastic-carbonate sequences: the Lower Triassic ramp succession of the transdanubian range, Hungary. Sediment. Geol. 395, 105549.

Hagdorn, H., Simon, T., 2021. Der Muschelkalk im nördlichen Baden-Württemberg. In: Hagdorn, H., Simon, T. (Eds.), Stratigraphie Von Deutschland XIII-Muschelkalk. Deutsche Stratigraphische Kommission, Subkommission Perm-Trias, Berlin, pp. 962–1006.

Harbaugh, J.W., 1967. Chapter 7 - carbonate oil reservoir rocks. In: George, V.C., Harold, J.B., Rhodes, W.F. (Eds.), Carbonate Rocks Origin, Occurrence and Classification. Elsevier, pp. 349–398.

Harlé, P., Kushnir, A.R.L., Aichholzer, C., Heap, M.J., Hehn, R., Maurer, V., Baud, P., Richard, A., Genter, A., Duringer, P., 2019. Heat flow density estimates in the Upper Rhine Graben using laboratory measurements of thermal conductivity on sedimentary rocks. Geotherm. Energy 7, 38.

Healy, D., 2023. https://github.com/DaveHealy-github/FracTend. (Accessed 1 April 2025).

Heap, M.J., Kushnir, A.R.L., Gilg, H.A., Violay, M.E.S., Harlé, P., Baud, P., 2019. Petrophysical properties of the muschelkalk from the Soultz-sous-Forêts geothermal site (France), an important lithostratigraphic unit for geothermal exploitation in the Upper Rhine Graben. Geotherm. Energy 7, 27.

Hemes, S., 2008. Strukturgeologische Kartierung des Muschelkalkausstrichs zwischen Wiesloch und Eschelbronn, im nördlichen Kraichgau (Baden-Württemberg), Geowissenschaftlichen Zentrum, Abteilungen Strukturgeologie und Angewandte Geologie. Georg-August-Universität, Göttingen, p. 89.

Hilgers, C., Dilg-Gruschinski, K., Urai, J.L., 2004. Microstructural evolution of syntaxial veins formed by advective flow. Geology 32, 261–264.

Honjo, S., Fischer, A.G., Garrison, R., 1965. Geopetal pyrite in fine-grained limestones. J. Sediment. Res. 35, 480–488.

Humphrey, E., Gomez-Rivas, E., Koehn, D., Bons, P.D., Neilson, J., Martín-Martín, J.D., Schoenherr, J., 2019. Stylolite-controlled diagenesis of a mudstone carbonate reservoir: a case study from the Zechstein-2-Carbonate (Central European Basin, NW Germany). Mar. Petrol. Geol. 109, 88–107.

Immenhauser, A., 2022. On the delimitation of the carbonate burial realm. Deposition. Record 8, 524–574.

Kaminskaite-Baranauskiene, I., Wang, H., Liu, Z., Li, H., 2023. Geothermal carbonate reservoirs and their sustainability: what can natural hydrothermal systems tell us? Geothermics 114, 102798.

Käßner, A., Tichomirowa, M., Rößler, R., Görz, I., 2024. Zircon U–Pb CA–ID–TIMS constraints on the chronology of the late carboniferous–early Permian continental döhlen Basin and its correlation with the thuringian forest basin (Central and Eastern Germany). Int. J. Earth Sci. 113, 1599–1618.

Kazmierczak, J., Coleman, M., Gruszczynski, M., Kempe, S., 1996. Cyanobacterial key to the genesis of micritic and peloidal limestones in ancient seas. Acta Palaeontol. Pol. 41, 319–338.

Khelifa, C., Zeddouri, A., Djabes, F., 2014. Influence of natural fractures on oil production of unconventional reservoirs. Energy Proc. 50, 360–367.

Kley, J., Voigt, T., 2008. Late Cretaceous intraplate thrusting in central Europe: effect of Africa-Iberia-Europe convergence, not alpine collision. Geology 36.

Klinkenberg, L.J., 1941. The permeability of porous media to liquids and gases. Drilling and Production Practice. American Petroleum Institute, pp. 200–213.

Knauth, L.P., 1979. A model for the origin of chert in limestone. Geology 7, 274–277.

Koehrer, B., Aigner, T., Forke, H., Pöppelreiter, M., 2012. Middle to Upper Khuff (Sequences KS1 to KS4) outcrop-equivalents in the Oman mountains: grainstone architecture on a subregional scale. GeoArabia (Manama) 17, 59–104.

Koehrer, B.S., Heymann, C., Prousa, F., Aigner, T., 2010. Multiple-scale facies and reservoir quality variations within a dolomite body – Outcrop analog study from the Middle Triassic, SW German Basin. Mar. Petrol. Geol. 27, 386–411.

Kosari, E., Kadkhodaie, A., Bahroudi, A., Chehrazi, A., Talebian, M., 2017. An integrated approach to study the impact of fractures distribution on the ilam-sarvak carbonate reservoirs: a case study from the strait of hormuz, the Persian Gulf. J. Petrol. Sci. Eng. 152, 104–115.

Kostic, E., Aigner, T., 2004. Sedimentary and poroperm anatomy of shoal-water carbonates (Muschelkalk, South-German Basin): an outcrop-analogue study of inter-well spacing scale. Facies 50, 113–131.

Kruszewski, M., Montegrossi, G., Saenger, E.H., 2023. The risk of fluid-injection-induced fault reactivation in carbonate reservoirs: an investigation of a geothermal system in the Ruhr region (Germany). Geomechan. Geophy. Geo-Energy Geo-Resour. 9, 38.

Kushnir, A.R.L., Heap, M.J., Baud, P., Gilg, H.A., Reuschlé, T., Lerouge, C., Dezayes, C., Duringer, P., 2018. Characterizing the physical properties of rocks from the Paleozoic to permo-triassic transition in the Upper Rhine Graben. Geotherm. Energy 6, 16.

Lamarche, J., Lavenu, A.,P.C., Gauthier, B.,D.M., Guglielmi, Y., Jayet, O., 2012. Relationships between fracture patterns, geodynamics and mechanical stratigraphy in carbonates (South-East Basin, France). Tectonophysics 581, 231–245.

Lander, R.H., Laubach, S.E., 2015. Insights into rates of fracture growth and sealing from a model for quartz cementation in fractured sandstones. GSA Bull. 127, 516–538.

Laubach, S.E., Olson, J.,E., Gale, J.,F.W., 2004. Are open fractures necessarily aligned with maximum horizontal stress? Earth Planet Sci. Lett. 222, 191–195.

LBEG, 2023. Underground gas storage in Germany. EEK 139, 41–49.

LGRB, 2022. L 6918-8 - Karte der mineralischen Rohstoffe 1 : 50 000 - Rohstoffvorkommen. Landesamt Für Geologie, Rohstoffe Und Bergbau.

Li, J.Z., Laubach, S.E., Gale, J.F.W., Marrett, R.A., 2018. Quantifying opening-mode fracture spatial organization in horizontal wellbore image logs, core and outcrop: application to Upper Cretaceous frontier formation tight gas sandstones, USA. J. Struct. Geol. 108, 137–156.

Longman, M.W., 1980. Carbonate diagenetic textures from nearsurface diagenetic environments 1. AAPG (Am. Assoc. Pet. Geol.) Bull. 64, 461–487.

Machel, H., 2005. Investigation of burial diagenesis in carbonate hydrocarbon reservoir rocks. Geosci. Can. 32, 103–128.

Macintyre, I.G., 1985. Submarine cements—The peloidal question. In: Schneidermann, N., Harris, P.M. (Eds.), Carbonate Cements: based on a symposium sponsored by the Society of Economic Paleontologists and Mineralogists. SEPM Society for Sedimentary Geology.

Marrett, R., Gale, J.,F.W., Gómez, L.,A., Laubach, S.,E., 2018. Correlation analysis of fracture arrangement in space. J. Struct. Geol. 108, 16–33.

Mattila, J., Tammisto, E., 2012. Stress-controlled fluid flow in fractures at the site of a potential nuclear waste repository, Finland. Geology 40, 299–302.

McKee, E.D., Gutschick, R.C., 1969. History of the Redwall Limestone of Northern Arizona. Geological Society of America.

Medici, G., Smeraglia, L., Torabi, A., Botter, C., 2021. Review of modeling approaches to groundwater flow in deformed carbonate aquifers. Groundwater 59, 334–351.

Mehl, J., 1982. Die Tempestit-Fazies im Oberen Muschelkalk Südbadens. Jahreshefte Geol. Landesamtes Baden-Wurttemberg 24, 91–109.

Meier, S., Bauer, J.,F., Philipp, S.,L., 2015. Fault zone characteristics, fracture systems and permeability implications of Middle Triassic muschelkalk in Southwest Germany. J. Struct. Geol. 70, 170–189.

Meixner, J., Schill, E., Gaucher, E., Kohl, T., 2014. Inferring the in situ stress regime in deep sediments: an example from the bruchsal geothermal site. Geotherm. Energy 2, 7.

Melzer, S., Budd, D., 2008. Retention of high permeability during shallow burial (300 to 500 m) of carbonate grainstones. J. Sediment. Res. - J Sediment Res 78, 548–561.

Merz, L., Bauer, U., Hilgers, C., 2019. Faults and fracture networks in Upper Muschelkalk outcrop analogues detected by photogrammetry, Upper Rhine Graben (URG), Germany. Poster presented at DGMK/ÖGEW Frühjahrstagung "Shaping the Energy Transitionwith Upstream and Storage Technologies" (2019), Celle, Deutschland, 25.–26. April 2019.

Merz, L., Manss, Y., Hilgers, C., 2018. Automated fracture analysis in Middle Triassic Muschelkalk, Upper Rhine Graben. Poster presented at DGMK/ÖGEW Frühjahrstagung "Shaping the Energy Transition with Upstream and Storage Technologies" (2018), Celle, Deutschland, 18.–19. April 2018.

Milliken, K.L., 1979. The silicified evaporite syndrome; two aspects of silicification history of former evaporite nodules from southern Kentucky and northern Tennessee. J. Sediment. Res. 49, 245–256.

Miocic, J.M., Girard, J.-P., Schöner, R., Gaupp, R., 2020. Mudstone/sandstone ratio control on carbonate cementation and reservoir quality in Upper Permian Rotliegend sandstones, offshore the Netherlands. Mar. Petrol. Geol. 115.

Monsees, A.,C., Busch, B., Schöner, N., Hilgers, C., 2020. Rock typing of diagenetically induced heterogeneities – a case study from a deeply-buried clastic Rotliegend reservoir of the Northern German Basin. Mar. Petrol. Geol. 113, 104163.

Moore H., C., Wade J., W., 2013. Chapter 11 - Natural fracturing in carbonate reservoirs. In: Moore H., C., Wade J., W. (Eds.), Carbonate Reservoirs. Elsevier, pp. 285–300.

Morris, A., Ferrill, D.A., Henderson, D.B., 1996. Slip-tendency analysis and fault reactivation. Geology 24, 275–278.

Narr, W., 1996. Estimating average fracture spacing in subsurface rock 1. AAPG (Am. Assoc. Pet. Geol.) Bull. 80, 1565–1585.

Ölmez, J.A., Busch, B., Hilgers, C., 2024. Reservoir quality of Upper Cretaceous limestones (Ahlen-Fm., Beckum Member, Münsterland Cretaceous Basin): effects of cementation and compaction on the compactable depositional volume. Int. J. Earth Sci.

Olson, J., Laubach, S., Lander, R., 2009. Natural fracture characterization in tight gas sandstones: integrating mechanics and diagenesis. AAPG (Am. Assoc. Pet. Geol.) Bull. 93, 1535–1549.

Panza, E., Agosta, F., Rustichelli, A., Zambrano, M., Tondi, E., Prosser, G., Giorgioni, M., Janiseck, J.M., 2016. Fracture stratigraphy and fluid flow properties of shallow-water, tight carbonates: the case study of the Murge Plateau (southern Italy). Mar. Petrol. Geol. 73, 350–370.

Petrovic, A., Aigner, T., 2017. Are shoal reservoirs discrete bodies? A coquina shoal outcrop analogue from the Mid-triassic upper muschelkalk, SW Germany. J. Petrol. Geol. 40, 249–275.

Pfaff, K., Hildebrandt, L.H., Leach, D.L., Jacob, D.E., Markl, G., 2010. Formation of the Wiesloch Mississippi Valley-type Zn-Pb-Ag deposit in the extensional setting of the Upper Rhinegraben, SW Germany. Miner. Deposita 45, 647–666.

Pierson, B., 2006. The control of cathodoluminescence in dolomite by iron and manganese. Sedimentology 28, 601–610.

Pöppelreiter, M., Simone, A., Hoetz, G., 2004. Reservoir characteristics of intercontinental carbonate ramp deposits-Upper muschelkalk, Middle Triassic, NE Netherlands. Netherlands J. Geosci./Geologie en Mijnbouw 83.

Pribnow, D., Schellschmidt, R., 2000. Thermal tracking of upper crustal fluid flow in the Rhine graben. Geophys. Res. Lett. 27, 1957–1960.

Questiaux, J.-M., Couples, G.D., Ruby, N., 2010. Fractured reservoirs with fracture corridors. Geophys. Prospect. 58, 279–295.

Rameil, N., 2008. Early diagenetic dolomitization and dedolomitization of late Jurassic and earliest Cretaceous platform carbonates: a case study from the Jura Mountains (NW Switzerland, E France). Sediment. Geol. 212, 70–85.

Rashid, F., Hussein, D., Lorinczi, P., Glover, P.W.J., 2023. The effect of fracturing on permeability in carbonate reservoir rocks. Mar. Petrol. Geol. 152, 106240.

Read, J.F., Antun, H., Michael, C., Clayton, W.L., Božo, P., 2016. Climate controlled, fabric destructive, reflux dolomitization and stabilization via marine- and synorogenic mixed fluids: an example from a large Mesozoic, calcite-sea platform, Croatia. Palaeogeogr. Palaeoclimatol. Palaeoecol. 449, 108–126.

Reinhold, C., Schwarz, M., Bruss, D., Heesbeen, B., Perner, M., Suana, M., 2016. The northern Upper Rhine graben–re-dawn of a mature petroleum province? Swiss. Bulletin 21, 35–56.

Rider, M., Kennedy, M., 2011. The Geological Interpretation of Well Logs, 3 ed. Rider-French Consulting Ltd., Scotland.

Rieckmann, M., 1970. Untersuchung von Turbulenzerscheinungen beim Fließen von Gasen durch Speichergesteine unter Berücksichtigung der Gleitströmung. Erdöl-Erdgas-Zeitschrift, Heft 2 (86), 36–51.

Roehl, P.O., Choquette, P.W., 2012. Carbonate Petroleum Reservoirs, 1 ed. Springer, New York, NY.

Rotstein, Y., Schaming, M., 2011. The Upper Rhine Graben (URG) revisited: Miocene transtension and transpression account for the observed first-order structures. Tectonics 30.

Ruf, M., Aigner, T., 2004. Facies and poroperm characteristics of a carbonate shoal (Muschelkalk, South German Basin): a reservoir analogue investigation. J. Petrol. Geol. 27, 215–239.

Schmidt, C., Busch, B., Hilgers, C., 2021. Lateral variations of detrital, authigenic and petrophysical properties in an outcrop analog of the fluvial plattensandstein, Lower Triassic, central S-Germany. Z. Dtsch. Ges. Geowiss. 172 (4), 541–564.

Schoenherr, J., Reuning, L., Hallenberger, M., Lüders, V., Lemmens, L., Biehl, B.,C., Lewin, A., Leupold, M., Wimmers, K., Strohmenger, C.,J., 2018. Dedolomitization: review and case study of uncommon mesogenetic formation conditions. Earth Sci. Rev. 185, 780–805.

Schumacher, M.E., 2002. Upper Rhine Graben: role of preexisting structures during rift evolution. Tectonics 21, 6-1-6-17.

Schwarz, M., Henk, A., 2005. Evolution and structure of the Upper Rhine Graben: insights from three-dimensional thermomechanical modelling. Int. J. Earth Sci. 94, 732–750.

Seufert, G., 1984. Lithostratigraphische Profile aus dem Trochitenkalk (Oberer Muschelkalk, mo1) des Kraichgaus und angrenzender Gebiete. Jahresber. Mittl. Oberrheinischen Geol. Vereins 66, 209–248.

Seufert, G., Schweizer, V., 1985. Stratigraphische und mikrofazielle Untersuchungen im Trochitenkalk (Unterer Hauptmuschelkalk, mo 1) des Kraichgaues und angrenzender Gebiete. Jahresber. Mittl. Oberrheinischen Geol. Vereins 67, 129–171.

Srivastava, D.,C., Lisle, R.,J., Imran, M., Kandpal, R., 1998. The kink-band triangle: a triangular plot for paleostress analysis from kink-bands. J. Struct. Geol. 20, 1579–1586.

Suski, B., Ladner, F., Baron, L., Vuataz, F.D., Philippossian, F., Holliger, K., 2008. Detection and characterization of hydraulically active fractures in a carbonate aquifer: results from self-potential, temperature and fluid electrical conductivity logging in the combioula hydrothermal system in the southwestern Swiss alps. Hydrogeol. J. 16, 1319–1328.

Tavakoli, V., 2020. Chapter 4 Macroscopic Heterogeneity - 4.2 Fractures, Carbonate Reservoir Heterogeneity - overcoming the challenges. Springer, Cham, pp. 73–76.

Terzaghi, R.D., 1965. Sources of error in joint surveys. Geotechnique 15, 287–304.

Toussaint, R., Aharonov, E., Koehn, D., Gratier, J.P., Ebner, M., Baud, P., Rolland, A., Renard, F., 2018. Stylolites: a review. J. Struct. Geol. 114, 163–195.

Vidal, J., Genter, A., 2018. Overview of naturally permeable fractured reservoirs in the central and southern Upper Rhine Graben: insights from geothermal wells. Geothermics 74, 57–73.

Vidal, J., Genter, A., Schmittbuhl, J., 2015. How do permeable fractures in the Triassic sediments of northern Alsace characterize the top of hydrothermal convective cells? Evidence from soultz geothermal boreholes (France). Geotherm. Energy 3, 8.

Villemin, T., Alvarez, F., Angelier, J., 1986. The Rhinegraben: extension, subsidence and shoulder uplift. Tectonophysics 128, 47–59.

Vollrath, A., 1938. Zur Stratigraphie und Bildung des Oberen Hauptmuschelkalkes in Mittel- und Westwürttemberg. Jahresber. Mittl. Oberrheinischen Geol. Vereins 27, 69–80.

Wagner Moreira, L., Tuany Younis Abdul, F., Maria Cordeiro do, C., Antonio Fernando Menezes, F., Luiz Antonio Pierantoni, G., 2023. Controls of fracturing on porosity in pre-salt carbonate reservoirs. Energy Geosci. 4, 100146.

Wang, Q., Laubach, S.E., Gale, J.F.W., Ramos, M.J., 2019. Quantified fracture (joint) clustering in Archean basement, Wyoming: application of the normalized correlation count method. Pet. Geosci. 25, 415–428.

Warnecke, M., Aigner, T., 2019. Asymmetry of an epicontinental basin—facies, cycles, tectonics and hydrodynamics: the Triassic Upper Muschelkalk, South Germanic Basin. Deposition. Record 5, 147–187.

Warren, J., 2000. Dolomite: occurrence, evolution and economically important associations. Earth Sci. Rev. 52, 1–81.

Worden, R., Armitage, P., Butcher, A., Churchill, J., Csoma, A., Hollis, C., Lander, R., Omma, J., 2018. Petroleum Reservoir Quality Prediction: Overview and Contrasting Approaches from Sandstone and Carbonate Communities, 435. Geological Society, London, Special Publications, pp. 1–31.

Zeeh, S., Geng, A., 2001. Origin and diagenesis of dolomite from the Muschelkalk Group (Middle Triassic) of SW Germany. Neues Jahrbuch fur Geologie und Palaontologie - Abhandlungen 221, 359–395.

Ziegler, P.,A., 1982. Geological Atlas of Western and Central Europe. Shell Internationale Petroleum Maatschapij B.V., The Hague, p. 239.

Ziegler, P.,A., 1992. European Cenozoic rift system. Tectonophysics 208, 91–111.